ACS ES&T Engineering

pubs.acs.org/estengg

Article

Feed Temperature Effects on Organic Fouling of Reverse Osmosis Membranes: Competition of Interfacial and Transport Properties

Sara BinAhmed, Raymond M. Hozalski, and Santiago Romero-Vargas Castrillón*

Cite This: https://dx.doi.org/10.1021/acsestengg.0c00258

Read Online

ACCESS | Metrics & More | Article Recommendations | Supporting Information

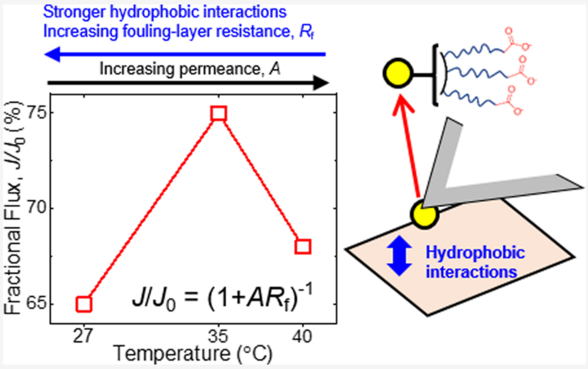

ABSTRACT: We investigated the effect of feedwater temperature on the organic fouling of reverse osmosis (RO) membranes. Experiments were conducted over the range $27 \leq T \leq 40$ °C, relevant to feed temperatures in arid, near-equatorial latitudes. Fouling by alginate, a major component of extracellular polymeric substances, was investigated at the nanoscale by means of AFM-based temperature-controlled colloidal-probe force spectroscopy (CPFS). The CPFS results, complemented by interfacial property characterization (contact angle, surface roughness, and charge) conducted under temperature-controlled conditions, enabled us to rationalize the observed fouling kinetics in cross-flow fouling experiments. We observed less severe flux loss at 35 °C ($J/J_0 = 75\%$, $t = 24$ h) compared to 27 °C ($J/J_0 = 65\%$), which is due to weaker adhesion forces with rising temperature. The observed variation in the magnitude of adhesion forces is consistent with the temperature dependence of hydrophobic interactions. At 40 °C, the observed flux loss ($J/J_0 = 68\%$) was similar to that at 27 °C, despite the fact that adhesion forces are relatively weak (and similar to those at 35 °C). Analysis using a series-resistance model shows that the foulant layer hydraulic resistance is equal at 35 and 40 °C, consistent with the CPFS results. More severe fouling was observed at 40 °C compared to 35 °C, however, due to the higher water permeance at 40 °C, which resulted in a greater flux of foulant to the membrane. Our experiments further show that the fouling layer develops within ∼2 h, during which the flux sharply decreases by 26% at 27 °C, 19% at 35 °C, and 22% at 40 °C; thereafter, flux losses are small and temperature independent. CPFS experiments show that this behavior is due to the foulant layer, which results in weak, often repulsive, and T-independent foulant—foulant interactions, which hinder further foulant deposition.

KEYWORDS: *reverse osmosis, hydrophobic interactions, fouling, wastewater reuse*

1. INTRODUCTION

Population growth and climate change are exerting enormous pressure on the world's water resources.[1−3] Over 2.4 billion people inhabit highly water stressed areas (defined as those with a water scarcity index > 0.4), many of which are in densely populated urban agglomerations in which water demand exceeds the watershed capacity.[4] In addition to increased population, urbanization, and industrialization,[5] climate change is expected to increase water stress through prolonged heatwaves that diminish surface and groundwater supplies.[6] There is thus an urgent need to tap into unconventional water sources (e.g., brackish water, seawater, and wastewater) to expand the water inventory.[2,7−9] Water recovered from secondary and tertiary municipal wastewater effluents can supplement water resources[10] through indirect use in agricultural and urban irrigation, cooling towers, and recharge of groundwater aquifers.[11] Desalination and advanced wastewater treatment by reverse osmosis (RO) have been instrumental in sustainably extracting potable water from unconventional water sources. Nonetheless, membrane fouling in its various forms (organic, inorganic, colloidal, biological) remains a key obstacle,[12−14] resulting in lower permeability and contaminant rejection,[1,12,14,15] ultimately increasing energy comsumption.[12]

Research over the past two decades has improved our understanding of the link between fouling propensity and RO membrane interfacial properties. Within the context of organic fouling of polyamide RO membranes, low roughness,[16] more hydrophilic,[17,18] and more negatively charged[19] membranes exhibit less pronounced flux losses.[16−19] Studies on the effect of feedwater quality have shown that Ca^{2+} causes more severe organic fouling (compared to Mg^{2+} and Na^{+}) with proteins (bovine serum albumin) and alginate,[20,21] likely due to the

Received: December 23, 2020
Revised: February 1, 2021
Accepted: February 9, 2021

calcium-mediated gelation of foulants[21−23] and Ca^{2+} bridging of carboxyl groups on the membrane and foulant.[20] A higher ionic strength results in compression of the electrical double layer and shielding of the surface charge of both the membrane and the foulants, resulting in a higher fouling rate due to a reduced electrostatic repulsion.[3,20,21] The effect of pH is more pronounced around the isoelectric point (IEP) of the foulant, such that foulant−membrane electrostatic repulsion is reduced and fouling rate increases at a pH equal to or less than the IEP of the foulant.[3,20,24] The presence of organic matter in water contributes to the formation of an organic fouling layer on the surface of the membrane, which can provide nutrients to bacteria and facilitate bacterial adhesion to the surface.[25−28] Therefore, minimizing organic fouling can help delay biofouling by mitigating initial bacterial adhesion to the surface of RO membranes.[29,30]

The influence of the feedwater temperature on membrane performance and fouling has attracted far less attention. Only a few studies have been devoted to this subject,[20,31−33] despite the increasing use of membrane-based desalination and wastewater reuse in arid, near-equatorial latitudes[34] where seawater temperatures can reach 35.5 °C.[35] Previous work on the connection between RO membrane transport properties and the feed temperature has shown that water permeability[32,36] increases with increasing temperature, due to lower water viscosity[37,38] and higher water diffusivity.[31,32] As a result of increasing temperature, permeate recovery increases[36,38−40] and energy consumption decreases due to lower pressure requirements.[39−41] Similarly, the salt permeability coefficient, B_s, is directly proportional to the solute diffusivity, D_s, and partition (solubility) coefficient K_s,[31,42,43] both of which increase with temperature, leading to a higher salt flux and lower salt rejection.[36,39,40,44] In one study, Goosen et al.[32] observed an increase in the permeate flux at a fixed applied pressure as the temperature was increased from 20 to 40 °C for NaCl concentrations ranging from 0 to 5% (w/v) NaCl, suggesting that the membrane undergoes morphological changes such as an increase in the polymer free void volume.[32] Sharma and Chellam[45] observed that the network pore size of nanofiltration (NF) membranes increased with increasing temperature (5−41 °C). In another study, Goosen et al.[33] found that correcting for viscosity changes of water with increasing temperature did not totally account for the increase in water permeance with increasing temperature. The researchers suggested an interplay between the feed temperature and the applied pressure that affected the membrane void volume. Francis and Pashley[38] observed that water recovery and permeate flow increased, while salt rejection decreased, with increasing temperature (20 to 30 °C) when treating seawater (0.5 M NaCl) and brackish water (0.2 M NaCl) with thin-film composite (TFC) RO membranes. Jin et al.[31] attributed the lower rejection of humic acid as total organic carbon (TOC) with increasing temperature (T = 15 to 35 °C) to increased swelling of the polymer network voids. The rates of fouling were similar at 25 and 35 °C while the highest flux decline occurred at 15 °C. The higher applied pressure and the larger size of humic acid aggregates at lower temperatures resulted in a higher resistance of the fouling layer at these temperatures.[31] On the other hand, Mo et al.[20] reported an increased rate of protein fouling (50 mg L^{-1} bovine serum albumin) of RO membranes at higher temperatures (18 to 35 °C) and for pH values 4.9 and 7. Baghdadi et al.[46] simulated the performance of two TFC RO membranes with increasing temperature (15−45 °C) and observed an increase in the salt mass transfer coefficient and a decrease in salt rejection when treating a 35 g L^{-1} NaCl feedwater at a constant hydraulic pressure (800 psi).

Current investigations of the effect of feedwater temperature on membrane performance are limited to bench-scale experiments, which describe thermal effects on membrane transport parameters and flux loss but offer little mechanistic insight.[20,31−33,46] To explain the connection between the feed temperature and the observed fouling kinetics, it is necessary to understand the thermal response of interfacial properties such as membrane hydrophobicity, roughness, and charge. As a step in this direction, we used colloidal probe atomic force microscopy (AFM) measurements to probe the effects of temperature on membrane−foulant and foulant−foulant interactions. We then explored how the temperature dependence of the interfacial properties manifests itself in RO membrane fouling experiments using alginate, a polysaccharide that is abundant in wastewater[47,48] and in bacterial biofilms,[49,50] as a model foulant. Our results show that weaker hydrophobic interactions with increasing feed temperature (from 27 to 35 °C) initially decrease membrane fouling, but further increases in feed temperature exacerbate fouling due to an increase in the water permeance of the membrane. Consequently, variation of the feed temperature reveals that fouling is determined by a competition between membrane interfacial and transport properties.

This paper is structured as follows. In Section 2, we describe the experimental protocols for the colloidal-probe AFM and dynamic fouling experiments. We discuss our results in Section 3, beginning with the effect of temperature (T) on interfacial properties (Section 3.1); the effect of T on foulant−membrane and foulant−foulant interactions, as determined by AFM, is discussed in Section 3.2; and Sections 3.3 and 3.4 present the results of membrane transport and fouling experiments, drawing connections to the interfacial and nanoscale adhesion properties. Concluding remarks are given in Section 4.

2. MATERIALS AND METHODS

2.1. Reverse Osmosis (RO) Membrane. All experiments were carried out with ESPA2-LD membranes (Hydranautics, Oceanside, CA), a low pressure aromatic polyamide RO membrane commonly employed in wastewater recycling.[10,51] Membrane coupons (~15 × 9 cm^2) were cut out from a 10 cm diameter spiral wound element (membrane area 7.43 m^2), rinsed in ultrapure water (UP) (18.2 MΩ cm, Barnstead), and stored at 5 °C in UP water. The hydraulic resistance and water permeance of the membranes were determined with a UP water feed at 25 °C. For quality assurance purposes, only membranes with A values within the range specified by the manufacturer (3.5−5.1 L m^{-2} h^{-1} bar^{-1}) were used for dynamic fouling experiments. Further details on the determination of membrane transport properties are provided in Section S.1 of the Supporting Information (SI).

The hydrophilicity and roughness of ESPA2-LD membranes were characterized at T = 27, 35, and 40 °C. Hydrophilicity was quantified in terms of water contact angle measurements in a temperature-controlled goniometer (DSA30S, Krüss). Both the temperature-controlled goniometer chamber and liquid dispenser were set to the same temperature, so that the droplet and substrate were in thermal equilibrium throughout the measurement. Root-mean-squared roughness (R_{RMS}) was measured in a temperature-controlled fluid cell using an atomic force microscope (MFP-3D-Bio, Asylum Research) in tapping mode. The zeta potential of the membrane was determined from streaming potential measurements using an electrokinetic analyzer (SurPass, Anton Paar). Streaming potential measurements were performed at 27 and 35 °C only (40 °C exceeded the maximum operating temperature of the instrument). Further details on membrane surface characterization are found in Section S.2 of the SI.

2.2. Organic Foulant and Feed Solution Chemistry.

We used alginate, a polysaccharide,[52] as a model foulant representative of extracellular polymeric substances (EPS)[53−56] in secondary wastewater effluent.[55−57] A 6 g L^{-1} sodium alginate (SA) (A2033, Millipore Sigma, St Louis, MO) stock solution was prepared in UP water before each dynamic fouling experiment by stirring the solution for 24 h. Alginate was dosed at a concentration of 250 mg L^{-1} to a feed solution containing 0.45 mM KH_2PO_4, 0.935 mM NH_4Cl, 0.5 mM $CaCl_2$, 0.5 mM $NaHCO_3$, 9.20 mM NaCl, and 0.61 mM $MgSO_4$ at pH 7.4. The inorganic composition of the synthetic wastewater used in all fouling experiments is representative of the inorganic fraction of secondary wastewater effluent from certain wastewater treatment plants in California.[50,58] The ionic strength of foulant-free synthetic wastewater was 14.7 mM (MinTEQ 3.1). The alginate concentration used (250 mg L^{-1}) is much higher than concentrations in real systems (in which TOC concentrations are in the 5−20 mg L^{-1} range[59−62]). An elevated concentration was used to accelerate fouling and ensure fouling can be observed within 24 h.

2.3. Dynamic Fouling Experiments.

A bench-scale crossflow system (see Section S.1) was used for fouling, with each experiment comprising the following stages: (1) Membrane compaction at 500−580 psi with UP water at 25 °C until a steady-state permeate flux was achieved. (2) Stabilization of the permeate flux at $J = 20 \pm 1$ L m^{-2} h^{-1} (LMH) for 1 h at 25 °C to validate the water permeance of the membrane (the manufacturer-specified water permeance for ESPA2-LD membranes is 3.5−5.1 LMH bar^{-1}). (3) Adjustment of the temperature of the UP feedwater to 27, 35, or 40 °C by means of a heater/chiller (6500 series, Polyscience) followed by overnight stabilization of the permeate flux at $J = 20 \pm 1$ LMH (this stage was used to calculate the A at each temperature). (4) Dosing of alginate-free synthetic wastewater into the feed tank, followed by system stabilization at the desired temperature (27, 35, or 40 °C) at $J = 20 \pm 1$ LMH; this stage typically required stabilization for 4−6 days, and included sampling of the feed and permeate conductivity to determine conductivity rejection before fouling. (5) Dosing of 250 mg L^{-1} alginate into the synthetic wastewater feed and initiation of dynamic fouling at an initial flux $J_0 = 20$ L m^{-2} h^{-1}; the flux loss during fouling was measured over 24 h accompanied by sampling of the feed and permeate conductivity and TOC content (2 and 24 h after initiation of fouling) to calculate conductivity and TOC rejection, respectively. The permeate flow rate was recorded every 0.2 s at all phases (except compaction) with a digital flow meter (SLI-2000, Sensirion, Stäfa, Switzerland) and logged to a computer. Further details on the experimental apparatus and fouling experiments can be found in the SI.

2.4. Colloidal Probe AFM Force Spectroscopy.

2.4.1. Colloidal Probes.

Carboxyl-modified latex (CML) colloidal particles with a nominal diameter of 4 μm were used in all AFM measurements. These polystyrene microspheres have a surface rich in carboxylic acid functional groups,[56,63] which are commonly found in alginate and other foulants.[56,64] According to the product specifications (ThermoFisher Scientific, C37253), the CML particles are hydrophobic at low pH and somewhat hydrophilic at high pH. However, other studies have characterized similar CML particles as hydrophobic.[65] CML particles were received as a 4% (w/v) suspension in deionized water and were stored at 5 °C until use.

2.4.2. Preparation of Colloidal Probes.

The protocol for preparing the colloidal probes was adapted from those reported by others.[3,63,66] A 20 μL aliquot of CML particle suspension (2500× dilution) was deposited on a UV/O_3-cleaned[67] glass slide and dried overnight in a desiccator. An inverted optical microscope (Zeiss Axio Observer A.1) integrated into the AFM was used to guide a tipless AFM cantilever (MLCT-O10 cantilever "A", nominal $k = 0.07$ N/m, Bruker) first toward a small amount of UV-curable glue (Norland 86, Norland optical, Cranbury, NJ) deposited on the glass slide and then toward the CML to be adhered to the cantilever. The prepared AFM colloidal probes were then cured in a solar simulator (xenon lamp, wavelength > 290 nm, 350 W/m^2) for 30 min.

2.4.3. Experimental Conditions.

The measurement of interfacial interactions between the CML probes and the surface of pristine and alginate-fouled ESPA2-LD membranes was performed using an atomic force microscope (MFP-3D-Bio, Asylum Research) equipped with a temperature-controlled fluid cell. Force measurements were conducted at $T = 27$ °C, 35 °C, and 40 °C in two different systems: pristine membranes in 20 mg L^{-1} alginate in synthetic wastewater (a concentration representative of the TOC levels of 5−20 mg L^{-1}[55,59] in wastewater effluent) and alginate-fouled membranes in synthetic wastewater supplemented with 20 mg L^{-1} alginate. The former investigates the temperature dependence of foulant−membrane interactions, which determine the initial adhesion of foulant at the early stages of fouling, while the latter measurements investigate foulant−foulant interactions in the subsequent stages, once a foulant layer has formed on the membrane surface.[3,63,68] Synthetic wastewater supplemented with 20 mg L^{-1} alginate was freshly prepared prior to each experiment as described in Section 2.2. The alginate-fouled membrane substrate was prepared as described in the SI (see Section S.1). To distinguish between real CML microsphere adhesion and artifacts resulting from particles contaminated with glue, control measurements were performed using a particle-free cantilever on which we deposited a small amount of cured glue. These measurements (performed in phosphate buffered saline at pH 7.4 on pristine membranes) resulted in distinctly sharp adhesion peaks compared to those of clean CML particles. Probes suspected of glue contamination were discarded. Only data collected with CML particles unaffected by glue artifacts are presented and discussed.

For individual coupons, force measurements were collected at 27 °C, then 35 °C, and finally 40 °C by ramping up the temperature at a rate of 1 °C/min. After allowing 30 min for the cantilever to reach thermal equilibrium, at each set-point temperature the inverse optical lever sensitivity and spring constant were determined (the latter according to the thermal noise method[69]). Measurements at the three temperatures were repeated in triplicate (i.e., with three different membrane coupons) with three independently functionalized AFM cantilevers. A total of ≥105 force curves were collected at each temperature. To account for membrane surface heterogeneity,[70] adhesion forces were measured at each temperature over at least 11 randomly selected spots (collecting three force curves per spot) located at least 6 μm apart from one another. The AFM probe was checked at the end of every experiment to verify that the CML particle was not dislocated and that it had remained at its original position during force measurements.

Force curves were recorded at a 200 nm/s approach−retraction speed, a cycle speed that results in negligible dissipative friction on the CML particle.[71] The CML probe engaged the membrane substrate with a trigger force (F_{trigger}; defined in Figure S3 of the SI) of 2 nN, while remaining in contact with the surface of the pristine or fouled membrane for a dwell time of 5 s. A constant force was maintained between the CML particle and membrane surface during the dwell time by setting the feedback channel to deflection. AFM experiments were performed in open-loop mode to minimize the noise in the collected forces. The choice of trigger force was based on calculations of the permeation drag force exerted on a 4-μm diameter particle experiencing a flux of 20 LMH, typical of RO operation (see Section S.3). For data analysis, the minimum measurable force—30 pN—was determined by measuring the noise in the free end of several force curves at each temperature. Parameters collected from the force curves are identified in Figure S3. From the extension force curve, the snap-in force (F_{snap}) is defined as the adhesion force observed as the colloidal probe approaches the membrane substrate;[72−74] snap-in separation (R_{snap}) is identified as the distance at which the snap-in event occurs.[75,76] From the retraction force curve, the peak adhesion force (F_{peak}) is defined as the maximum adhesion force observed as the colloidal probe is pulled away from the membrane; the rupture separation (R) is the distance at which interactions between the probe and the membrane surface vanish.[77]

2.5. Statistical Analysis. Unpaired two-sided homoscedastic (equal variance) *t*-tests were used to determine the statistical significance of the results.

3. RESULTS AND DISCUSSION

3.1. Characterization of the RO Membrane. The contact angle of sessile water droplets (θ_w) reflects membrane hydrophilicity[78−80] and depends on membrane properties (surface roughness, surface charge, and surface functional groups)[78,80−82] as well as on external conditions such as the water temperature[78,83] and salt concentration.[78,84] The effect of temperature on θ_w and the root-mean-squared roughness (R_{RMS}) of pristine RO membranes is shown in Figure 1. The measured θ_w at 27 °C (53.5 ± 2.5°) is similar to that reported by other studies (43°−55°)[10,85] on ESPA2 membranes at room temperature. The contact angle at 27 °C was significantly higher than that at 35 °C (38.5 ± 2.8°; $p < 0.01$) and at 40 °C (36.7 ± 3.5°; $p < 0.01$), but the θ_w values at 35 and 40 °C were similar ($p = 0.078$). The decrease in the contact angle with increasing temperature is a manifestation of a general surface phenomenon: as first postulated by Zisman[86] and Petke and Ray,[87] θ_w decreases with rising T for common liquids whose surface tension decreases with increasing T. It is expected that the membrane would swell more at higher temperatures, as has been observed with polyamide membranes,[31,88] due to the increasing wettability of the membrane by water. Consistent with this expectation, we observed (Figure 1) an increase in R_{RMS} of the pristine RO membrane with increasing temperature (representative AFM scans at each T are given in Figure S1). R_{RMS} increased from 91.8 ± 12.3 nm at 27 °C to 113.7 ± 15.7 nm at 35 °C ($p < 0.01$) and 102.8 ± 14.5 nm at 40 °C ($p < 0.05$), while the R_{RMS} values at 35 and 40 °C were similar ($p = 0.0562$).

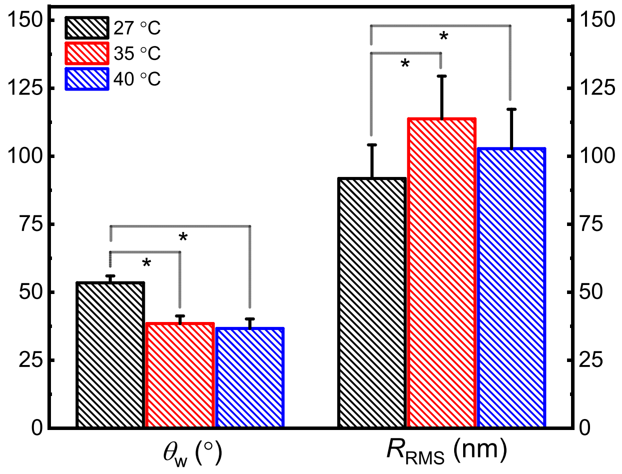

Figure 1. Sessile water drop contact angle (θ_w) and root-mean-squared roughness (R_{RMS}) measurements of pristine ESPA2-LD membranes at T = 27, 35, and 40 °C (* denotes a significant difference between the indicated samples, $p < 0.05$).

The zeta potential (ζ) of ESPA2-LD membranes at 27 °C (Figure S2) varied from −7 mV to −35 mV as the pH was increased from 4 to 10 with $\zeta \approx -30$ mV at pH = 7.4. The negative charge of polyamide is due to the deprotonation of carboxylic acid groups on the membrane surface[84] and presumably to the adsorption of hydroxide ions on uncharged hydrophobic regions on polyamide. Hydroxide ion adsorption is posited as the cause of the negative charge of many hydrophobic surfaces.[89,90] At 27 and 35 °C we observe a similar charging behavior at pH < 7, while a less negative ζ is observed at a basic pH at 35 °C. We ascribe this behavior to a lower extent of adsorption of hydroxide ions resulting from the decreasing hydrophobicity of the interface at 35 °C (cf. Figure 1).

3.2. Effect of Temperature on Adhesion Forces. In this section, we investigate the T dependence of membrane surface forces using AFM-based force spectroscopy measurements with a carboxylated colloidal probe (a mimic of alginate). We considered pristine membranes as well as alginate-fouled membranes (prepared as explained in the SI) to investigate the T dependence of foulant−membrane and foulant−foulant interactions. Previous work has used AFM to relate foulant−membrane interactions to the rate of fouling, finding a strong correlation between the fouling propensity and the strength of adhesion forces determined by AFM.[56,63] On the other hand, the effect of temperature, investigated below, has hitherto been overlooked. We analyzed both the approach and the retraction segments of the force curves. The approach segment provides information about the mechanism of the adhesion of foulant molecules as they first encounter the membrane interface, i.e., whether foulants experience repulsive or attractive forces during initial adhesion (and the strength of such interactions). The retraction segment quantifies the force necessary to detach adhered foulants.

Before discussing the force spectroscopy data quantitatively (Figures 2, 3, and S6−S9), a few qualitative features of the force curves are noteworthy. Figures S3 and S4 show

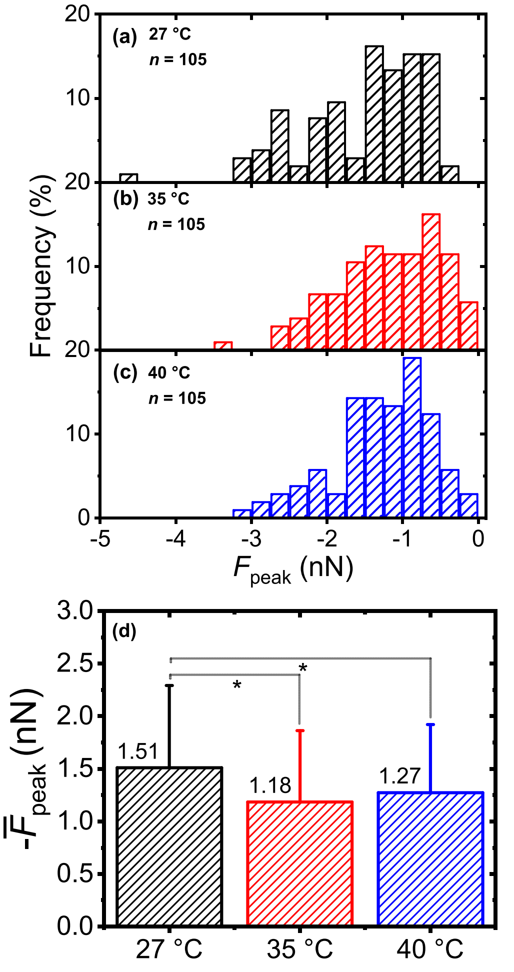

Figure 2. (a−c) Distribution of peak adhesion forces (F_{peak}) of CML colloidal probes on pristine ESPA2-LD membranes for each indicated temperature (given in the inset along with the number of force measurements, n). (d) Average peak adhesion force ($\overline{F}_{\mathrm{peak}}$) at each temperature calculated from (a)−(c) (* denotes statistical significance with $p < 0.05$). Error bars denote one standard deviation. Data were collected in synthetic wastewater supplemented with 20 mg L^{-1} sodium alginate (t_{contact} = 5 s; F_{trigger} = 2 nN; pH 7.4; I = 14.7 mM).

representative force−distance curves, including the approach segment as the inset, collected over pristine and alginate-fouled membranes, respectively. The CML microsphere experiences a small repulsive force ($F_{\mathrm{rep}} \sim$ 43−50 pN; see Figure S3) as it approaches the surface of the pristine membranes; this repulsion is likely steric as it is observed at separations (8−9 nm) greater than the Debye length (2.5 nm at I = 14.7 mM). At shorter separations, the polystyrene chains on the microsphere surface eventually encounter the surface, and the microsphere experiences a sudden attractive force known as a "snap-in" or "jump-to-contact" spring instability:[91,92] at the snap-in point, the gradient of the particle−membrane force exceeds the cantilever spring constant, the cantilever becomes unstable (i.e., the particle−surface force and the cantilever elastic force are no longer in balance), and jump-to-contact occurs. This jump-to-contact force has been attributed to the van der Waals attractive force between the tip and the surface.[72−74] The snap-in force is not observed in the approach force curves recorded over alginate-fouled membranes (inset in Figure S4a,b); instead, the force is repulsive throughout the contact region, but the gradual increase in the loading force is consistent with compression of the soft alginate layer by the colloidal microsphere.[76] The retraction force curves over pristine membranes display sharp (often multiple) adhesion peaks (Figure S3), presumed to be due to the stretching of polystyrene chains upon probe pull-off. In some cases, we observe tethering events (Figure S5a,b), which are likely due to the detachment of alginate molecules bridging (with the aid of $\mathrm{Ca^{2+}}$) the CML probe and the membrane surface[93] or desorption[94] of alginate molecules from the membrane. Over alginate-fouled membranes, we observe adhesion peaks, likely due to alginate desorption (Figure S4a). In addition, a fraction of the force curves (quantified below) are repulsive during retraction (Figure S4b), indicating that the alginate layer prevented the adhesion events that are otherwise observed in pristine membranes.

Next, we discuss quantitatively the force spectroscopy data in terms of the distribution of peak adhesion, snap-in forces, and rupture separations (defined in Section 2.4.3 and in Figure S3). The data are plotted as histograms in Figures 2, 3, and S6−S9. The distribution of snap-in forces (F_{snap}) and snap-in separations (R_{snap}) on pristine membranes is shown in Figures S6 and S7. As shown in Figure S6d, the attraction is strongest at 27 °C when the membrane is least hydrophilic and smoothest (see Figure 1), with an average snap-in force ($\overline{F}_{\mathrm{snap}}$) of 115 pN compared to 81 pN at 35 °C (p = 0.039) and 92 pN at 40 °C (p = 0.138). The force curves that do not display a snap-in force (i.e., purely repulsive approach curves tallied as the "NO" column in Figures S6a−c), representing between 31.4% and 45.7% of the forces, were assigned F_{snap} = 0 when calculating the average in Figure S6d. A similar trend—decreasing $\overline{F}_{\mathrm{snap}}$ with rising T —is observed when the average excluded the nonadhesive approaches, Figure S6e. The probability with which snap-in events occurred (ranging between 54.3% and 68.6%) and the distance at which snap-in is established (R_{snap}, Figure S7), ∼8−9 nm on average, showed no discernible T dependence.

Figure 2a−c shows the peak adhesion force (F_{peak}) distribution (defined in Figure S3) of the CML probes collected over pristine membranes at T = 27, 35, and 40 °C. The distribution of the F_{peak} at 27 °C shows more frequent strong adhesion events (-3 nN $< F_{\mathrm{peak}} < -2$ nN) compared to higher temperatures. Moreover, Figure 2d shows that the average adhesion force at 27 °C ($\overline{F}_{\mathrm{peak}} = -1.51 \pm 0.78$ nN) is stronger than those at 35 °C ($\overline{F}_{\mathrm{peak}} = -1.18 \pm 0.68$ nN; p = 0.0015) and 40 °C ($\overline{F}_{\mathrm{peak}} = -1.27 \pm 0.65$ nN; p = 0.0174). Adhesion forces at 35 and 40 °C were similar (p = 0.339), which is consistent with the invariant contact angle and surface roughness at these same temperatures (cf. Figure 1). We expect adhesion forces to decrease at $T > 40$ °C, as observed by other studies.[95,96] Such a range, however, is not environmentally relevant and was therefore not studied in our work. The distribution of rupture separations (R) over pristine membranes (Figure S8), ranging between 120 and 150 nm, was not dependent on T.

The decreasing adhesion force with increasing temperature observed during approach (F_{snap}; Figure S6) and retraction (F_{peak}; Figure 2) followed the same trend with T as the hydrophobic interactions, suggesting that the T dependence of organic foulant adhesion shows close resemblance to hydrophobic hydration phenomena. Weakening of hydrophobic adhesion forces with rising T agree with previous force spectroscopic experiments.[95,96] The decreasing magnitude of adhesion forces is also consistent with theoretical inves-

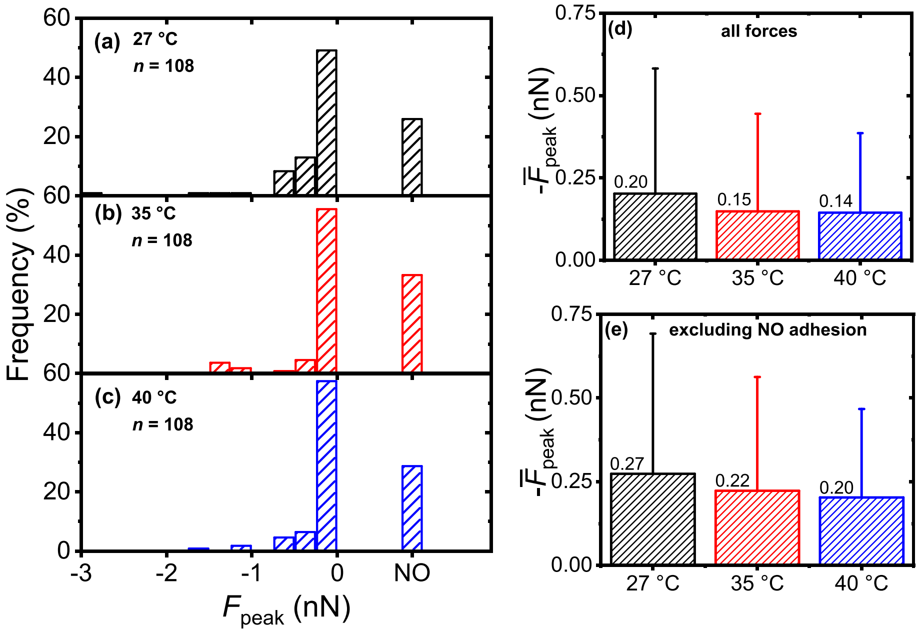

Figure 3. (a−c) Distribution of peak adhesion forces (F_{peak}) of CML colloidal probes on alginate-fouled ESPA2-LD membranes for each indicated temperature (given in the inset along with the number of force measurements, n). Force curves in which $|F_{peak}| < 30$ pN are tallied as the "NO" column (30 pN is the magnitude of the noise observed in the free end of force curves). (d) Average peak adhesion force ($\overline{F}_{peak}$) at each temperature calculated from (a)−(c) including the nonadhesive events as $\overline{F}_{peak} = 0$. (e) Average peak adhesion force ($\overline{F}_{peak}$) at each temperature calculated from (a)−(c) excluding the nonadhesive events. Error bars denote one standard deviation. Data were collected in synthetic wastewater supplemented with 20 mg L^{-1} sodium alginate ($t_{contact} = 5$ s; $F_{trigger} = 2$ nN; pH 7.4; $I = 14.7$ mM).

tigations showing that macroscopic surfaces become less hydrophobic with rising T.[97] As first envisaged by Stillinger,[98] hydration of large hydrophobes requires the formation of a water-depleted interface around the solute, akin to a liquid−vapor interface. Building on these ideas, Chandler and coworkers showed that the free energy of hydrophobic solvation scales with the liquid−vapor surface tension of water (γ) as $\Delta G \sim 4\pi\gamma R^2$ (where R is the hydrophobic solute radius).[99] Accordingly, the temperature dependence of ΔG approaches that of γ (i.e., it decreases with rising temperature), with hydrophobic hydration becoming more energetically favorable at higher T.[97]

While hydrophobic interactions appear to be the main driving force of foulant−membrane adhesion, we cannot rule out the possibility that adhesion is aided by Ca^{2+}-mediated[13,63] bridging interactions between the deprotonated carboxylic groups on the CML particle and the surface of the membrane. Both the membrane (Figure S2) and alginate are negatively charged at pH > 6 because most of the carboxylic groups are deprotonated[93] (pK_a = 3.5−4.7[3,16,100]). The presence of deprotonated carboxylic acid groups is suggested by the negative charge of both the membrane (Figure S2) and alginate.[16,93]

Substantially different surface forces dominate the interactions between the colloidal particle and the alginate-fouled membrane. These results are presented in Figure 3a−c for T = 27, 35, and 40 °C, respectively. As mentioned previously, snap-in events are absent in measurements with fouled membranes; we observe instead repulsive forces during approach at any temperature (see Figure S4). Repulsive forces are also observed in 25.9−33.3% of the retraction force curves (denoted by the "NO" column in Figure 3a−c). These repulsive forces can be attributed to strong electrostatic repulsion between the CML particle and the more negative membrane surface in the presence of the alginate fouling layer.[101] Wang et al.[68] also attributed weaker alginate−alginate adhesion forces to electrostatic repulsive forces resulting from the more negative charge of alginate compared to other foulants (bovine serum albumin and effluent organic matter). In contrast to the pristine membrane, the average peak adhesion force ($\overline{F}_{peak}$) over fouled membranes is significantly weaker in magnitude and less sensitive to temperature ($p > 0.05$ for all pairwise comparisons) irrespective of whether repulsive forces curves are included in the average (Figure 3d) or not (Figure 3e).

The distribution of rupture separations (R) of CML particles over fouled membranes at T = 27, 35, and 40 °C is shown in Figure S9. Although $\overline{R}$ is similar for all the temperatures investigated ($p > 0.05$ for all pairwise comparisons), $\overline{R}$ has a larger value (≈ 0.6 μm) on the fouled membranes than on pristine membranes (compare Figure S9 with Figure S8). Longer rupture separations are likely due to desorption of alginate molecules from the membrane surface during probe retraction.

3.3. Effect of Temperature on Membrane Transport Parameters.

Having established the T-dependence of membrane adhesive properties, we next examine the impact of T on transport and selectivity during membrane filtration. The effect of temperature on the membrane permeance to water and conductivity rejection of ESPA2-LD thin-film composite membranes is shown in Figure 4.

In agreement with previous experiments (5 °C < T < 60 °C),[32,39,102] A increases with the feed temperature (Figure 4) from 3.8 ± 0.3 LMH bar^{-1} at 27 °C to 4.9 ± 0.4 and 6.7 ± 0.8 LMH bar^{-1} at 35 and 40 °C, respectively. The change in permeance with temperature is due to the dependence of A on water viscosity and diffusivity:[31,39] $A \propto \frac{D_{w,m}}{T}$ ($D_{w,m}$ is the water

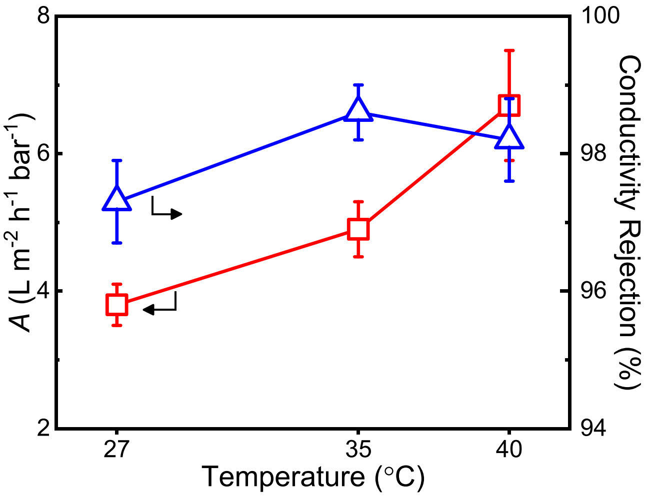

Figure 4. Effect of temperature on the permeance to water (A) and conductivity rejection (right y-axis) of ESPA2-LD membranes at T = 27, 35, and 40 °C. The error bars denote one standard deviation. Alginate-free synthetic wastewater feed was used to determine conductivity rejection (number of measurements n = 6 at 27 °C, n = 6 at 35 °C, and n = 8 at 40 °C). All data determined at a permeate flux J = 20 ± 1 LMH.

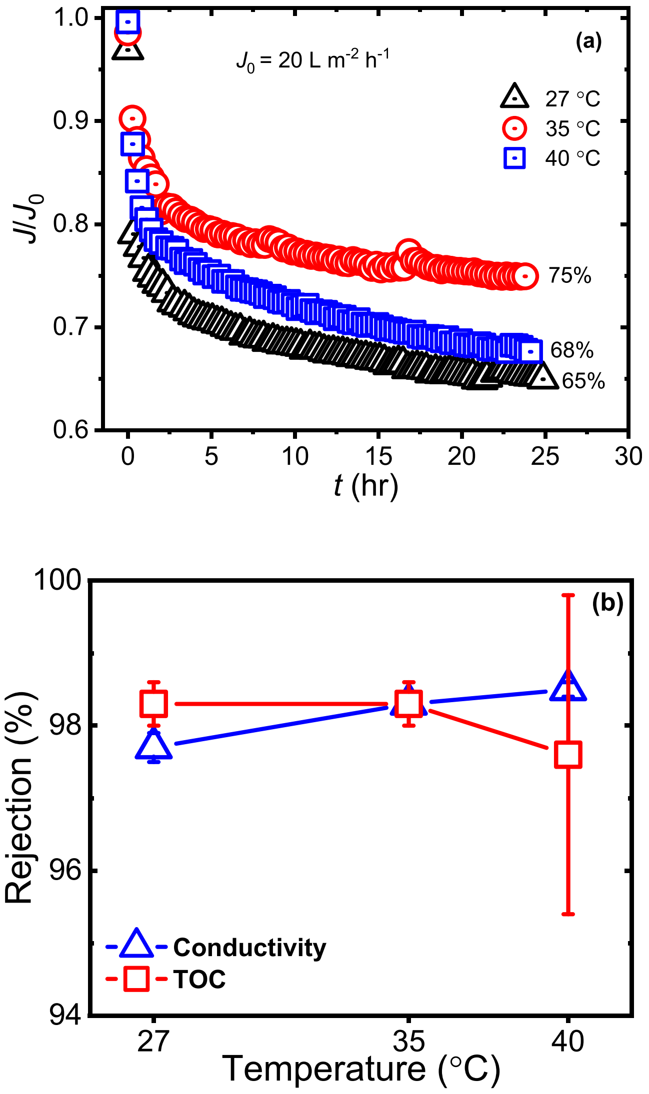

Figure 5. Effect of temperature on the performance of ESPA2-LD membranes during alginate fouling: (a) flux decline of ESPA2-LD membranes over 24 h during accelerated fouling with 250 mg L^{-1} sodium alginate for each indicated feed temperature given in the inset. Due to the noise underlying the permeate flow rate measurements, flux data was smoothed using a locally estimated scatterplot smoothing algorithm (loess) implemented in Origin 2018 (Northampton, MA). (b) Average conductivity and TOC rejection after initiation of fouling. Error bars denote one standard deviation. Experimental conditions: initial permeate flux J_0 = 20 LMH; synthetic wastewater feed (I = 14.7 mM) at pH = 7.4 supplemented with 250 mg L^{-1} sodium alginate; crossflow velocity = 15.8 cm s^{-1}.

diffusivity in the membrane) and $D_{\mathrm{w,m}} \propto \frac{T}{\mu}$ (μ is the dynamic water viscosity).[31] As a result, A will be inversely proportional to μ which, in turn, varies inversely with temperature.[36,102,103] Another possible factor contributing to the increase in A is the thermal expansion of the polyamide network:[31] the increase in surface roughness with T (Figure 1) is presumably due to thermal expansion of the polyamide active layer.[31] In addition, the increase in roughness observed between 27 and 35 °C (Figure 1)—resulting in a larger effective permeable area[104]—may also be responsible for the increase in A[105] observed between 27 and 35 °C.

Conductivity rejection was found to be weakly dependent on T, ranging from 97.3 ± 0.6% at 27 °C to 98.6 ± 0.4% and 98.2 ± 0.6% at 35 and 40 °C, respectively. While these observations are at odds with the expected temperature dependence of the solute diffusivity, D_s, and solubility, K_s, in the membrane (both D_s and K_s increase with increasing temperature),[31,39,106] the results in Figure 4 appear to be in agreement with other studies showing negligible temperature dependence of the reflection coefficient over a similar temperature range.[32]

3.4. Effect of Temperature on Organic Fouling. The effect of temperature on alginate fouling is investigated in Figure 5a, showing the normalized permeate flux, J/J_0, as a function of time. The time dependence of the permeate flux exhibits common features at all temperatures, indicative of a transition of fouling dominated by foulant−membrane interactions to a regime determined by foulant−foulant interactions.[107] A steep flux loss (26% at 27 °C, 19% at 35 °C, and 22% at 40 °C) within the first 2 h is followed by slow flux decline at longer times (Figure 5a). This behavior is consistent with our colloidal AFM data: at short time scales, fouling is dominated by strong foulant−clean membrane interactions (Figures 2 and S6), leading to the rapid formation of a foulant layer and significant flux loss. At longer times scales ($t \gtrsim$ 2 h), weakly adhesive or repulsive foulant−foulant interactions (Figure 3) cause J/J_0 to decrease at a much slower rate. On the other hand, the extent of the flux loss is different at each temperature. Fouling is most severe at 27 °C, with a flux loss of 35% after 24 h compared to 25% at 35 °C and 32% at 40 °C. The more significant fouling at 27 °C is consistent with the stronger hydrophobic interactions at this temperature (cf. Figure 2). However, at 35 and 40 °C different fouling propensity does not reflect the similar adhesion forces observed in Figure 2. Thus, interfacial behavior alone does not explain the observed fouling behavior.

To reconcile the fouling experiments in Figure 5a with the interfacial behavior presented in Figure 2, we quantified the resistance contributed by the foulant layer to water transport using a resistance-in-series model.[108,109] Within this approach, the overall transport resistance of the fouled membrane is given by the sum of the individual hydraulic resistances of the polyamide (A^{-1}) and a (time-dependent) hydraulic resistance due to the foulant layer, $A_f(t)^{-1}$. The resulting expression for the time-dependent flux through the fouled membrane is

$$J(t) = \frac{1}{A^{-1} + A_f(t)^{-1}}(\Delta p - \Delta\pi) \tag{1}$$

where $\Delta\pi$ is the osmotic pressure difference between the feed and the permeate. Dividing eq 1 by the steady-state water flux through the clean membrane [$J_0 = A(\Delta p - \Delta\pi)$] yields

$$\frac{J(t)}{J_0} = \frac{1}{1 + \frac{A}{A_f(t)}} = \frac{1}{1 + R_f(t)A} \tag{2}$$

where the inverse of the permeability of the foulant layer is expressed as a hydraulic resistance, $R_f(t) = A_f(t)^{-1}$. Equation 1 shows that two mechanisms could contribute to flux loss: fouling, which increases $R_f(t)$ as the foulant layer develops, and increasing water permeance (e.g., due to T), which will also lower J/J_0 due to the increased convective flux of foulant to the membrane. Based on the characterization results, we speculate that the smaller flux loss at 35 °C compared to 27 °C is primarily due to the effect of the interfacial properties on the foulant layer: a lower R_f value at 35 °C results from a thinner foulant layer due to a more hydrophilic membrane (Figure 1) and weaker hydrophobic interactions (Figure 2) at 35 °C versus 27 °C. The smaller R_f mitigates the effect of a larger value of A at 35 °C compared to 27 °C (Figure 4), with the net effect being a smaller flux loss at 35 °C. Conversely, raising T from 35 to 40 °C brings about a negligible change in interfacial properties and R_f (similar hydrophilicity and adhesion forces, cf. Figures 1 and 2), but a significant increase in A (Figure 4) that results in more severe flux loss at 40 °C compared to 35 °C.

These arguments are supported by the experimental data. Solving for R_f using eq 2 with data from Figures 4 and 5 ($A_{35°\mathrm{C}}$ = 4.9 LMH bar^{-1}, $A_{40°\mathrm{C}}$ = 6.7 LMH bar^{-1}, $(J(t = 24\ \mathrm{h})/J_0)_{35°\mathrm{C}}$ = 0.75 and $(J(t = 24\ \mathrm{h})/J_0)_{40°\mathrm{C}}$ = 0.68) yields $R_{f,35°\mathrm{C}}$ = 0.07 bar LMH^{-1} = $R_{f,40°\mathrm{C}}$, i.e., similar foulant layer resistances consistent with the AFM results (Figure 2); thus, the greater flux loss at 40 °C compared to 35 °C stems from $A_{40°\mathrm{C}} > A_{35°\mathrm{C}}$ (Figure 4). On the other hand, $R_{f,27°\mathrm{C}}$ = 0.14 bar LMH^{-1}, a significantly higher resistance (due to stronger adhesion at 27 °C) that causes a more pronounced flux loss compared to experiments at higher T. As we elaborate in Section S.4 (SI), we estimate the thickness of the foulant layer at $O(10\ \mu\mathrm{m})$ and the fraction of foulant adhered to the membrane at ca. 3% of the total mass of alginate. Thus, we can neglect the contribution to the slow-down of the fouling rate resulting from a lower concentration of alginate in the feed.

Finally, the results of conductivity and TOC rejection at each temperature are summarized in Figure 5b. These data are derived from measurements at t = 2 and 24 h after initiation of the fouling experiment and are reported as a single average as they were similar (within 1%) to one another at each temperature. Conductivity rejection remained approximately constant with increasing temperature, exhibiting values similar to those of the clean membrane (see Figure 4). Similarly, TOC rejection shown in Figure 5b is independent of temperature. Although increased passage of dissolved alginate could be expected with rising temperature on account of membrane swelling,[31] the high TOC rejection suggests that alginate (likely found as Ca^{2+}-complexed aggregates) is large enough (>1 nm,[110] compared to subnanometer voids in polyamide[1,105]) to deposit on the surface of the membrane as a fouling layer. The TOC passage observed (1.7–2.4%) is likely due to low molecular weight impurities in alginate (e.g., polyphenols and proteins[111]). A similar TOC passage has been observed by previous studies with humic acid.[31]

4. CONCLUSION

We have shown that membrane interfacial and transport properties play competing roles during alginate fouling of reverse osmosis membranes at different temperatures. Colloidal probe force spectroscopy (CPFS) measurements show that foulant–membrane interactions are markedly temperature-dependent (Figure 2). Rising temperature *weakens* foulant adhesion, given that foulant–membrane hydrophobic interactions, which become weaker with increasing temperature, drive adhesion onto clean membranes. Conversely, the monotonic increase in water permeance with temperature (Figure 4) worsens fouling, which suggests that lower operating pressures (and hence lower fluxes) will be needed during extreme temperature conditions (e.g., heat waves) to avoid exposing the membrane to excessive fouling. Interestingly, our results suggest that membrane hydrophilicity, a key interfacial property in membrane development, becomes less relevant at high feed temperatures, since membranes become *ipso facto* less hydrophobic at higher temperatures (Figures 1 and 2). CPFS measurements further show that the alginate layer is self-limiting: once an adlayer of a critical thickness is formed, deposition of additional foulant molecules is hindered by weak (or repulsive) foulant–foulant interactions (Figure 3), which appear to be temperature independent. Our results also suggest possible lines for future inquiry. Understanding of the process conditions that lead to the formation of the critical foulant layer is crucial for effective fouling management. Given the preeminent role of hydrophobic interactions in alginate fouling, experiments at lower temperatures (which strengthen foulant–membrane hydrophobic interactions) should be conducted to understand fouling under feed conditions relevant to temperate and cold climates. These experiments would also be useful in the formulation of cleaning-in-place formulations tailored to specific feedwater temperatures.

■ ASSOCIATED CONTENT

Supporting Information

The Supporting Information is available free of charge at https://pubs.acs.org/doi/10.1021/acsestengg.0c00258.

Additional materials and methods (Sections S.1 and S.2); calculation of the permeate drag force exerted on a colloidal particle (Section S.3); estimation of the foulant layer thickness and adsorbed mass (Section S.4); tapping-mode AFM images of polyamide membranes at various temperatures (Figure S1); ζ-potential of polyamide membranes at various temperature and pH conditions (Figure S2); representative force curves over pristine and alginate-fouled membranes (Figures S3–S5); snap-in forces (Figure S6) and snap-in distances (Figure S7) on pristine membranes; and rupture separations over pristine (Figure S8) and alginate-fouled (Figure S9) membranes (PDF)

AUTHOR INFORMATION

Corresponding Author

Santiago Romero-Vargas Castrillón − *Department of Civil, Environmental, and Geo- Engineering, University of Minnesota, Minneapolis, Minnesota 55455, United States; Institute for Infrastructure and Environment, School of Engineering and Institute for Materials and Processes, School of Engineering, The University of Edinburgh, Edinburgh EH9 3FG, United Kingdom;* orcid.org/0000-0003-3339-7692; Phone: +44(0)131 651 3567; Email: santiago@ed.ac.uk, sromerov@umn.edu

Authors

Sara BinAhmed − *Department of Civil, Environmental, and Geo- Engineering, University of Minnesota, Minneapolis, Minnesota 55455, United States*

Raymond M. Hozalski − *Department of Civil, Environmental, and Geo- Engineering, University of Minnesota, Minneapolis, Minnesota 55455, United States;* orcid.org/0000-0002-7541-0165

Complete contact information is available at:
https://pubs.acs.org/10.1021/acsestengg.0c00258

Notes

The authors declare no competing financial interest.

ACKNOWLEDGMENTS

This work was supported by grants to S.R.-V.C. from 3M Co. (Non-Tenured Faculty Award) and the Environment and Natural Resources Trust Fund, as recommended by the Legislative-Citizen Commission on Minnesota Resources. We thank Hydranautics (Oceanside, CA) for supplying the membranes used in the initial stages of this investigation. The technical assistance of Wieslaw J. Suszynski (Coating Process Fundamentals Visualization Laboratory, University of Minnesota) with contact angle measurements is gratefully acknowledged. S.B.-A. acknowledges support from the Graduate School at the University of Minnesota through a Doctoral Dissertation Fellowship. S.R.-V.C. is grateful to Dr. Steve Jons (Dupont Water Solutions) for useful comments regarding the series-resistance model.

REFERENCES

(1) Werber, J. R.; Osuji, C. O.; Elimelech, M. Materials for Next-Generation Desalination and Water Purification Membranes. *Nat. Rev. Mater.* **2016**, *1*, 1−15.

(2) Jjemba, P. K.; Weinrich, L. A.; Cheng, W.; Giraldo, E.; LeChevallier, M. W. Regrowth of Potential Opportunistic Pathogens and Algae in Reclaimed-Water Distribution Systems. *Appl. Environ. Microbiol.* **2010**, *76* (13), 4169−4178.

(3) Ang, W. S.; Elimelech, M. Protein (BSA) Fouling of Reverse Osmosis Membranes: Implications for Wastewater Reclamation. *J. Membr. Sci.* **2007**, *296* (1−2), 83−92.

(4) Oki, T.; Kanae, S. Global Hydrological Cycles and World Water Resources. *Science (Washington, DC, U. S.)* **2006**, *313* (5790), 1068−1072.

(5) Gullinkala, T.; Escobar, I. C. Membranes for Water Treatment Applications - An Overview. *ACS Symp. Ser.* **2011**, *1078*, 155−170.

(6) Kelley, C. P.; Mohtadi, S.; Cane, M. A.; Seager, R.; Kushnir, Y. Climate Change in the Fertile Crescent and Implications of the Recent Syrian Drought. *Proc. Natl. Acad. Sci. U. S. A.* **2015**, *112* (11), 3241−3246.

(7) Alvarez, P. J. J.; Chan, C. K.; Elimelech, M.; Halas, N. J.; Villagrán, D. Emerging Opportunities for Nanotechnology to Enhance Water Security. *Nat. Nanotechnol.* **2018**, *13* (8), 634−641.

(8) Elimelech, M.; Phillip, W. A. The Future of Seawater Desalination: Energy, Technology, and the Environment. *Science (Washington, DC, U. S.)* **2011**, *333* (6043), 712−717.

(9) Jarusutthirak, C.; Amy, G. Membrane Filtration of Wastewater Effluents for Reuse: Effluent Organic Matter Rejection and Fouling. *Water Sci. Technol.* **2001**, *43* (10), 225−232.

(10) Fujioka, T.; Khan, S. J.; McDonald, J. A.; Henderson, R. K.; Poussade, Y.; Drewes, J. E.; Nghiem, L. D. Effects of Membrane Fouling on N-Nitrosamine Rejection by Nanofiltration and Reverse Osmosis Membranes. *J. Membr. Sci.* **2013**, *427*, 311−319.

(11) Petala, M.; Tsiridis, V.; Samaras, P.; Zouboulis, A.; Sakellaropoulos, G. P. Wastewater Reclamation by Advanced Treatment of Secondary Effluents. *Desalination* **2006**, *195*, 109−118.

(12) Doederer, K.; Farré, M. J.; Pidou, M.; Weinberg, H. S.; Gernjak, W. Rejection of Disinfection By-Products by RO and NF Membranes: Influence of Solute Properties and Operational Parameters. *J. Membr. Sci.* **2014**, *467*, 195−205.

(13) Wu, J.; Contreras, A. E.; Li, Q. Studying the Impact of RO Membrane Surface Functional Groups on Alginate Fouling in Seawater Desalination. *J. Membr. Sci.* **2014**, *458*, 120−127.

(14) Kang, G.; Cao, Y. Development of Antifouling Reverse Osmosis Membranes for Water Treatment: A Review. *Water Res.* **2012**, *46* (3), 584−600.

(15) Varin, K. J.; Lin, N. H.; Cohen, Y. Biofouling and Cleaning Effectiveness of Surface Nanostructured Reverse Osmosis Membranes. *J. Membr. Sci.* **2013**, *446*, 472−481.

(16) Li, Q.; Xu, Z.; Pinnau, I. Fouling of Reverse Osmosis Membranes by Biopolymers in Wastewater Secondary Effluent: Role of Membrane Surface Properties and Initial Permeate Flux. *J. Membr. Sci.* **2007**, *290* (1−2), 173−181.

(17) Xu, P.; Drewes, J. E.; Kim, T.-U.; Bellona, C.; Amy, G. Effect of Membrane Fouling on Transport of Organic Contaminants in NF/RO Membrane Applications. *J. Membr. Sci.* **2006**, *279* (1−2), 165−175.

(18) Zou, L.; Vidalis, I.; Steele, D.; Michelmore, A.; Low, S. P.; Verberk, J. Q. J. C. Surface Hydrophilic Modification of RO Membranes by Plasma Polymerization for Low Organic Fouling. *J. Membr. Sci.* **2011**, *369* (1−2), 420−428.

(19) Ghanbari, M.; Emadzadeh, D.; Lau, W. J.; Matsuura, T.; Ismail, A. F. Synthesis and Characterization of Novel Thin Film Nanocomposite Reverse Osmosis Membranes with Improved Organic Fouling Properties for Water Desalination. *RSC Adv.* **2015**, *5* (27), 21268−21276.

(20) Mo, H.; Tay, K. G.; Ng, H. Y. Fouling of Reverse Osmosis Membrane by Protein (BSA): Effects of PH, Calcium, Magnesium, Ionic Strength and Temperature. *J. Membr. Sci.* **2008**, *315*, 28−35.

(21) Lee, S.; Ang, W. S.; Elimelech, M. Fouling of Reverse Osmosis Membranes by Hydrophilic Organic Matter: Implications for Water Reuse. *Desalination* **2006**, *187*, 313−321.

(22) Ang, W. S.; Lee, S.; Elimelech, M. Chemical and Physical Aspects of Cleaning of Organic-Fouled Reverse Osmosis Membranes. *J. Membr. Sci.* **2006**, *272* (1−2), 198−210.

(23) Katsoufidou, K.; Yiantsios, S. G.; Karabelas, A. J. An Experimental Study of UF Membrane Fouling by Humic Acid and Sodium Alginate Solutions: The Effect of Backwashing on Flux Recovery. *Desalination* **2008**, *220* (1−3), 214−227.

(24) Jones, K. L.; O'Melia, C. R. Ultrafiltration of Protein and Humic Substances: Effect of Solution Chemistry on Fouling and Flux Decline. *J. Membr. Sci.* **2001**, *193* (2), 163−173.

(25) Bazaka, K.; Jacob, M. V.; Crawford, R. J.; Ivanova, E. P. Efficient Surface Modification of Biomaterial to Prevent Biofilm Formation and the Attachment of Microorganisms. *Appl. Microbiol. Biotechnol.* **2012**, *95* (2), 299−311.

(26) Friedlander, R. S.; Vogel, N.; Aizenberg, J. Role of Flagella in Adhesion of *Escherichia Coli* to Abiotic Surfaces. *Langmuir* **2015**, *31* (22), 6137−6144.

(27) Garrett, T. R.; Bhakoo, M.; Zhang, Z. Bacterial Adhesion and Biofilms on Surfaces. *Prog. Nat. Sci.* **2008**, *18* (9), 1049−1056.

(28) Araújo, E. A.; de Andrade, N. J.; da Silva, L. H. M.; de Carvalho, A. F.; de Sá Silva, C. A.; Ramos, A. M. Control of Microbial Adhesion as a Strategy for Food and Bioprocess Technology. *Food Bioprocess Technol.* **2010**, *3* (3), 321−332.

(29) Baek, Y.; Yu, J.; Kim, S.-H.; Lee, S.; Yoon, J. Effect of Surface Properties of Reverse Osmosis Membranes on Biofouling Occurrence under Filtration Conditions. *J. Membr. Sci.* **2011**, *382* (1−2), 91−99.

(30) Suwarno, S. R.; Hanada, S.; Chong, T. H.; Goto, S.; Henmi, M.; Fane, A. G. The Effect of Different Surface Conditioning Layers on Bacterial Adhesion on Reverse Osmosis Membranes. *Desalination* **2016**, *387*, 1−13.

(31) Jin, X.; Jawor, A.; Kim, S.; Hoek, E. M. V. V. Effects of Feed Water Temperature on Separation Performance and Organic Fouling of Brackish Water RO Membranes. *Desalination* **2009**, *239* (1−3), 346−359.

(32) Goosen, M. F. A.; Sablani, S. S.; Al-Maskari, S. S.; Al-Belushi, R. H.; Wilf, M. Effect of Feed Temperature on Permeate Flux and Mass Transfer Coefficient in Spiral-Wound Reverse Osmosis Systems. *Desalination* **2002**, *144* (1−3), 367−372.

(33) Goosen, M. F. A. A.; Sablani, S.; Cin, M. D.; Wilf, M. Effect of Cyclic Changes in Temperature and Pressure on Permeation Properties of Composite Polyamide Seawater Reverse Osmosis Membranes. *Sep. Sci. Technol.* **2010**, *46* (1), 14−26.

(34) Kim, S.; Lee, S.; Lee, E.; Sarper, S.; Kim, C. H.; Cho, J. Enhanced or Reduced Concentration Polarization by Membrane Fouling in Seawater Reverse Osmosis (SWRO) Processes. *Desalination* **2009**, *247* (1−3), 162−168.

(35) John, V. C.; Coles, S. L.; Abozed, A. I. Seasonal Cycles of Temperature, Salinity and Water Masses of the Western Arabian Gulf. *Oceanol. Acta* **1990**, *13* (3), 273−282.

(36) Agashichev, S. P.; Lootahb, K. N. Influence of Temperature and Permeate Recovery on Energy Consumption of a Reverse Osmosis System. *Desalination* **2003**, *154* (3), 253−266.

(37) Schaep, J.; Van Der Bruggen, B.; Uytterhoeven, S.; Croux, R.; Vandecasteele, C.; Wilms, D.; Van Houtte, E.; Vanlerberghe, F. Remvoal of Hardness from Groundwater by Nanofiltration. *Desalination* **1998**, *119* (1−3), 295−301.

(38) Francis, M. J. J.; Pashley, R. M. M. The Effects of Feed Water Temperature and Dissolved Gases on Permeate Flow Rate and Permeate Conductivity in a Pilot Scale Reverse Osmosis Desalination Unit. *Desalin. Water Treat.* **2011**, *36* (1−3), 363−373.

(39) Jawor, A.; Hoek, E. M. V. Effects of Feed Water Temperature on Inorganic Fouling of Brackish Water RO Membranes. *Desalination* **2009**, *235* (1−3), 44−57.

(40) Al-Mutaz, I. S.; Al-Ghunaimi, M. A. Performance of Reverse Osmosis Units at High Temperatures. Presented at *IDA World Congress on Desalination and Water Reuse*, 2001.

(41) Wilf, M.; Bartels, C. Optimization of Seawater RO Systems Design. *Desalination* **2005**, *173* (1), 1−12.

(42) Geise, G. M.; Park, H. B.; Sagle, A. C.; Freeman, B. D.; McGrath, J. E. Water Permeability and Water/Salt Selectivity Tradeoff in Polymers for Desalination. *J. Membr. Sci.* **2011**, *369* (1−2), 130−138.

(43) Geise, G. M.; Paul, D. R.; Freeman, B. D. Fundamental Water and Salt Transport Properties of Polymeric Materials. *Prog. Polym. Sci.* **2014**, *39*, 1−24.

(44) Ormanci-Acar, T.; Celebi, F.; Keskin, B.; Mutlu-Salmanlı, O.; Agtas, M.; Turken, T.; Tufani, A.; Imer, D. Y.; Ince, G. O.; Demir, T. U.; et al. Fabrication and Characterization of Temperature and PH Resistant Thin Film Nanocomposite Membranes Embedded with Halloysite Nanotubes for Dye Rejection. *Desalination* **2018**, *429*, 20−32.

(45) Sharma, R. R.; Chellam, S. Temperature Effects on the Morphology of Porous Thin Film Composite Nanofiltration Membranes. *Environ. Sci. Technol.* **2005**, *39* (13), 5022−5030.

(46) Baghdadi, Y. N.; Alnouri, S. Y.; Matsuura, T.; Tarboush, B. J. A. Temperature Effects on Concentration Polarization Thickness in Thin-Film Composite Reverse Osmosis Membranes. *Chem. Eng. Technol.* **2018**, *41* (10), 1905−1912.

(47) Listiarini, K.; Chun, W.; Sun, D. D.; Leckie, J. O. Fouling Mechanism and Resistance Analyses of Systems Containing Sodium Alginate, Calcium, Alum and Their Combination in Dead-End Fouling of Nanofiltration Membranes. *J. Membr. Sci.* **2009**, *344* (1−2), 244−251.

(48) Romero-Vargas Castrillón, S.; Lu, X.; Shaffer, D. L.; Elimelech, M. Amine Enrichment and Poly(Ethylene Glycol) (PEG) Surface Modification of Thin-Film Composite Forward Osmosis Membranes for Organic Fouling Control. *J. Membr. Sci.* **2014**, *450*, 331−339.

(49) Boyd, A.; Chakrabarty, A. M. Pseudomonas Aeruginosa Biofilms: Role of the Alginate Exopolysaccharide. *J. Ind. Microbiol.* **1995**, *15* (3), 162−168.

(50) Herzberg, M.; Elimelech, M. Biofouling of Reverse Osmosis Membranes: Role of Biofilm-Enhanced Osmotic Pressure. *J. Membr. Sci.* **2007**, *295* (1−2), 11−20.

(51) Bellona, C.; Heil, D.; Yu, C.; Fu, P.; Drewes, J. E. The Pros and Cons of Using Nanofiltration in Lieu of Reverse Osmosis for Indirect Potable Reuse Applications. *Sep. Purif. Technol.* **2012**, *85*, 69−76.

(52) Ci, S. X.; Huynh, T. H.; Louie, L. W.; Yang, A.; Beals, B. J.; Ron, N.; Tsang, W.-G.; Soon-Shiong, P.; Desai, N. P. Molecular Mass Distribution of Sodium Alginate by High-Performance Size-Exclusion Chromatography. *J. Chromatogr. A* **1999**, *864* (2), 199−210.

(53) Ye, Y.; Le Clech, P.; Chen, V.; Fane, A. G.; Jefferson, B. Fouling Mechanisms of Alginate Solutions as Model Extracellular Polymeric Substances. *Desalination* **2005**, *175* (1), 7−20.

(54) Matin, A.; Shafi, H.; Wang, M.; Khan, Z.; Gleason, K.; Rahman, F. Reverse Osmosis Membranes Surface-Modified Using an Initiated Chemical Vapor Deposition Technique Show Resistance to Alginate Fouling under Cross-Flow Conditions: Filtration & Subsequent Characterization. *Desalination* **2016**, *379*, 108−117.

(55) Katsoufidou, K.; Yiantsios, S. G.; Karabelas, A. J. Experimental Study of Ultrafiltration Membrane Fouling by Sodium Alginate and Flux Recovery by Backwashing. *J. Membr. Sci.* **2007**, *300* (1−2), 137−146.

(56) Lu, X.; Romero-Vargas Castrillón, S.; Shaffer, D. L.; Ma, J.; Elimelech, M. In Situ Surface Chemical Modification of Thin-Film Composite Forward Osmosis Membranes for Enhanced Organic Fouling Resistance. *Environ. Sci. Technol.* **2013**, *47* (21), 12219.

(57) Ang, W. S.; Yip, N. Y.; Tiraferri, A.; Elimelech, M. Chemical Cleaning of RO Membranes Fouled by Wastewater Effluent: Achieving Higher Efficiency with Dual-Step Cleaning. *J. Membr. Sci.* **2011**, *382* (1−2), 100−106.

(58) Tiraferri, A.; Kang, Y.; Giannelis, E. P.; Elimelech, M. Superhydrophilic Thin-Film Composite Forward Osmosis Membranes for Organic Fouling Control: Fouling Behavior and Antifouling Mechanisms. *Environ. Sci. Technol.* **2012**, *46* (20), 11135−11144.

(59) Bartels, C. R.; Wilf, M.; Andes, K.; Iong, J. Design Considerations for Wastewater Treatment by Reverse Osmosis. *Water Sci. Technol.* **2005**, *51* (6−7), 473−482.

(60) Khan, M. T.; Busch, M.; Molina, V. G.; Emwas, A.-H.; Aubry, C.; Croue, J.-P. How Different Is the Composition of the Fouling Layer of Wastewater Reuse and Seawater Desalination RO Membranes? *Water Res.* **2014**, *59*, 271−282.

(61) Kim, H.-C.; Dempsey, B. A. Comparison of Two Fractionation Strategies for Characterization of Wastewater Effluent Organic Matter and Diagnosis of Membrane Fouling. *Water Res.* **2012**, *46* (11), 3714−3722.

(62) Michael-Kordatou, I.; Michael, C.; Duan, X.; He, X.; Dionysiou, D. D.; Mills, M. A.; Fatta-Kassinos, D. Dissolved Effluent Organic Matter: Characteristics and Potential Implications in Wastewater Treatment and Reuse Applications. *Water Res.* **2015**, *77*, 213−248.

(63) Li, Q.; Elimelech, M. Organic Fouling and Chemical Cleaning of Nanofiltration Membranes: Measurements and Mechanisms. *Environ. Sci. Technol.* **2004**, *38* (17), 4683−4693.

(64) Mi, B.; Elimelech, M. Organic Fouling of Forward Osmosis Membranes: Fouling Reversibility and Cleaning without Chemical Reagents. *J. Membr. Sci.* **2010**, *348* (1−2), 337−345.

(65) Behrens, S. H.; Christl, D. I.; Emmerzael, R.; Schurtenberger, P.; Borkovec, M. Charging and Aggregation Properties of Carboxyl Latex Particles: Experiments versus DLVO Theory. *Langmuir* **2000**, *16* (6), 2566−2575.

(66) Beaussart, A.; El-Kirat-Chatel, S.; Sullan, R. M. A.; Alsteens, D.; Herman, P.; Derclaye, S.; Dufrêne, Y. F. Quantifying the Forces Guiding Microbial Cell Adhesion Using Single-Cell Force Spectroscopy. *Nat. Protoc.* **2014**, *9* (5), 1049−1055.

(67) Zhang, X. H.; Quinn, A.; Ducker, W. A. Nanobubbles at the Interface between Water and a Hydrophobic Solid. *Langmuir* **2008**, *24* (9), 4756−4764.

(68) Wang, L.; Miao, R.; Wang, X.; Lv, Y.; Meng, X.; Yang, Y.; Huang, D.; Feng, L.; Liu, Z.; Ju, K. Fouling Behavior of Typical Organic Foulants in Polyvinylidene Fluoride Ultrafiltration Membranes: Characterization from Microforces. *Environ. Sci. Technol.* **2013**, *47* (8), 3708−3714.

(69) Hutter, J. L.; Bechhoefer, J. Calibration of Atomic-Force Microscope Tips. *Rev. Sci. Instrum.* **1993**, *64* (7), 1868−1873.

(70) Allen, A.; Semião, A. J. C.; Habimana, O.; Heffernan, R.; Safari, A.; Casey, E. Nanofiltration and Reverse Osmosis Surface Topographical Heterogeneities: Do They Matter for Initial Bacterial Adhesion? *J. Membr. Sci.* **2015**, *486*, 10−20.

(71) Lo, Y.-S.; Simons, J.; Beebe, T. P. Temperature Dependence of the Biotin-Avidin Bond-Rupture Force Studied by Atomic Force Microscopy. *J. Phys. Chem. B* **2002**, *106* (38), 9847−9852.

(72) Heinz, W. F.; Hoh, J. H. Getting Physical with Your Chemistry: Mechanically Investigating Local Structure and Properties of Surfaces with the Atomic Force Microscope. *J. Chem. Educ.* **2005**, *82* (5), 695−703.

(73) Heinz, W. F.; Hoh, J. H. Spatially Resolved Force Spectroscopy of Biological Surfaces Using the Atomic Force Microscope. *Trends Biotechnol.* **1999**, *17* (4), 143−150.

(74) Erts, D.; Lõhmus, A.; Lõhmus, R.; Olin, H.; Pokropivny, A. V.; Ryen, L.; Svensson, K. Force Interactions and Adhesion of Gold Contacts Using a Combined Atomic Force Microscope and Transmission Electron Microscope. *Appl. Surf. Sci.* **2002**, *188* (3−4), 460−466.

(75) Thewes, N.; Loskill, P.; Jung, P.; Peisker, H.; Bischoff, M.; Herrmann, M.; Jacobs, K. Hydrophobic Interaction Governs Unspecific Adhesion of Staphylococci: A Single Cell Force Spectroscopy Study. *Beilstein J. Nanotechnol.* **2014**, *5*, 1501−1512.

(76) Butt, H.-J.; Cappella, B.; Kappl, M. Force Measurements with the Atomic Force Microscope: Technique, Interpretation and Applications. *Surf. Sci. Rep.* **2005**, *59* (1), 1−152.

(77) Binahmed, S.; Hasane, A.; Wang, Z.; Mansurov, A.; Romero-Vargas Castrillón, S. Bacterial Adhesion to Ultrafiltration Membranes: Role of Hydrophilicity, Natural Organic Matter, and Cell-Surface Macromolecules. *Environ. Sci. Technol.* **2018**, *52* (1), 162−172.

(78) Li, Q.; Pan, X.; Qu, Z.; Zhao, X.; Jin, Y.; Dai, H.; Yang, B.; Wang, X. Understanding the Dependence of Contact Angles of Commercially RO Membranes on External Conditions and Surface Features. *Desalination* **2013**, *309*, 38−45.

(79) Akin, O.; Temelli, F. Probing the Hydrophobicity of Commercial Reverse Osmosis Membranes Produced by Interfacial Polymerization Using Contact Angle, XPS, FTIR, FE-SEM and AFM. *Desalination* **2011**, *278* (1−3), 387−396.

(80) Miller, D. J.; Dreyer, D. R.; Bielawski, C. W.; Paul, D. R.; Freeman, B. D. Surface Modification of Water Purification Membranes. *Angew. Chem., Int. Ed.* **2017**, *56* (17), 4662−4711.

(81) Andrade, J. D.; Smith, L. M.; Gregonis, D. E. The Contact Angle and Interface Energetics. In *Surface and Interfacial Aspects of Biomedical Polymers*; Springer US: Boston, MA, 1985; Vol. *1*, pp 249−292; DOI: 10.1007/978-1-4684-8610-0_7.

(82) Surawanvijit, S.; Rahardianto, A.; Cohen, Y. An Integrated Approach for Characterization of Polyamide Reverse Osmosis Membrane Degradation Due to Exposure to Free Chlorine. *J. Membr. Sci.* **2016**, *510*, 164−173.

(83) Diaz, M. E.; Savage, M. D.; Cerro, R. L. The Effect of Temperature on Contact Angles and Wetting Transitions for N-Alkanes on PTFE. *J. Colloid Interface Sci.* **2017**, *503*, 159−167.

(84) Yang, J.; Lee, S.; Lee, E.; Lee, J.; Hong, S. Effect of Solution Chemistry on the Surface Property of Reverse Osmosis Membranes under Seawater Conditions. *Desalination* **2009**, *247* (1−3), 148−161.

(85) Tu, K. L.; Chivas, A. R.; Nghiem, L. D. Effects of Chemical Preservation on Flux and Solute Rejection by Reverse Osmosis Membranes. *J. Membr. Sci.* **2014**, *472*, 202−209.

(86) Zisman, W. A. Relation of the Equilibrium Contact Angle to Liquid and Solid Constitution. *Adv. Chem. Ser.* **1964**, *43*, 1−51.

(87) Petke, D. F.; Ray, R. B. Temperature Dependence of Contact Angles of Liquids on Polymeric Solids. *J. Colloid Interface Sci.* **1969**, *31* (2), 216−227.

(88) Nilsson, M.; Trägårdh, G.; Östergren, K. The Influence of PH, Salt and Temperature on Nanofiltration Performance. *J. Membr. Sci.* **2008**, *312* (1−2), 97−106.

(89) Kasemset, S.; He, Z.; Miller, D. J.; Freeman, B. D.; Sharma, M. M. Effect of Polydopamine Deposition Conditions on Polysulfone Ultrafiltration Membrane Properties and Threshold Flux during Oil/Water Emulsion Filtration. *Polymer* **2016**, *97*, 247−257.

(90) Kudin, K. N.; Car, R. Why Are Water-Hydrophobic Interfaces Charged? *J. Am. Chem. Soc.* **2008**, *130* (12), 3915−3919.

(91) Seo, Y.; Jhe, W. Atomic Force Microscopy and Spectroscopy. *Rep. Prog. Phys.* **2008**, *71* (1), 016101.

(92) Thewes, N.; Thewes, A.; Loskill, P.; Peisker, H.; Bischoff, M.; Herrmann, M.; Santen, L.; Jacobs, K. Stochastic Binding of Staphylococcus Aureus to Hydrophobic Surfaces. *Soft Matter* **2015**, *11* (46), 8913−8919.

(93) Lee, S.; Elimelech, M. Relating Organic Fouling of Reverse Osmosis Membranes to Intermolecular Adhesion Forces. *Environ. Sci. Technol.* **2006**, *40* (3), 980−987.

(94) Kocun, M.; Grandbois, M.; Cuccia, L. A. Single Molecule Atomic Force Microscopy and Force Spectroscopy of Chitosan. *Colloids Surf., B* **2011**, *82* (2), 470−476.

(95) Stock, P.; Utzig, T.; Valtiner, M. Direct and Quantitative AFM Measurements of the Concentration and Temperature Dependence of the Hydrophobic Force Law at Nanoscopic Contacts. *J. Colloid Interface Sci.* **2015**, *446*, 244−251.

(96) Dallin, B. C.; Yeon, H.; Ostwalt, A. R.; Abbott, N. L.; Van Lehn, R. C. Molecular Order Affects Interfacial Water Structure and Temperature-Dependent Hydrophobic Interactions between Nonpolar Self-Assembled Monolayers. *Langmuir* **2019**, *35* (6), 2078−2088.

(97) Huang, D. M.; Chandler, D. Temperature and Length Scale Dependence of Hydrophobic Effects and Their Possible Implications for Protein Folding. *Proc. Natl. Acad. Sci. U. S. A.* **2000**, *97* (15), 8324−8327.

(98) Stillinger, F. H. Structure in Aqueous Solutions of Nonpolar Solutes from the Standpoint of Scaled-Particle Theory. *J. Solution Chem.* **1973**, *2* (2−3), 141−158.

(99) Huang, D. M.; Geissler, P. L.; Chandler, D. Scaling of Hydrophobic Solvation Free Energies. *J. Phys. Chem. B* **2001**, *105* (28), 6704−6709.

(100) Elimelech, M.; Childress, A. E. *Zeta Potential of Reverse Osmosis Membranes: Implications for Membrane Performance*; National Technical Reports Library: 1996.

(101) Jermann, D.; Pronk, W.; Meylan, S.; Boller, M. Interplay of Different NOM Fouling Mechanisms during Ultrafiltration for Drinking Water Production. *Water Res.* **2007**, *41* (8), 1713−1722.

(102) Mehdizadeh, H.; Dickson, J. M.; Eriksson, P. K. Temperature Effects on the Performance of Thin-Film Composite, Aromatic Polyamide Membranes. *Ind. Eng. Chem. Res.* **1989**, *28* (6), 814−824.

(103) Madaeni, S. S.; Mansourpanah, Y. Chemical Cleaning of Reverse Osmosis Membranes Fouled by Whey. *Desalination* **2004**, *161* (1), 13−24.

(104) Karan, S.; Jiang, Z.; Livingston, A. G. Sub-10 Nm Polyamide Nanofilms with Ultrafast Solvent Transport for Molecular Separation. *Science (Washington, DC, U. S.)* **2015**, *348* (6241), 1347−1351.

(105) Fujioka, T.; Oshima, N.; Suzuki, R.; Price, W. E.; Nghiem, L. D. Probing the Internal Structure of Reverse Osmosis Membranes by Positron Annihilation Spectroscopy: Gaining More Insight into the Transport of Water and Small Solutes. *J. Membr. Sci.* **2015**, *486*, 106−118.

(106) Goh, P. S.; Lau, W. J.; Othman, M. H. D.; Ismail, A. F. Membrane Fouling in Desalination and Its Mitigation Strategies. *Desalination* **2018**, *425*, 130−155.

(107) Liu, J.; Huang, T.; Ji, R.; Wang, Z.; Tang, C. Y.; Leckie, J. O. Stochastic Collision-Attachment-Based Monte Carlo Simulation of Colloidal Fouling: Transition from Foulant-Clean-Membrane Interaction to Foulant-Fouled-Membrane Interaction. *Environ. Sci. Technol.* **2020**, *54* (19), 12703−12712.

(108) Henis, J. M. S.; Tripodi, M. K. Composite Hollow Fiber Membranes for Gas Separation: The Resistance Model Approach. *J. Membr. Sci.* **1981**, *8* (3), 233−246.

(109) Sagle, A. C.; Van Wagner, E. M.; Ju, H.; McCloskey, B. D.; Freeman, B. D.; Sharma, M. M. PEG-Coated Reverse Osmosis Membranes: Desalination Properties and Fouling Resistance. *J. Membr. Sci.* **2009**, *340*, 92.

(110) Ang, W. S.; Tiraferri, A.; Chen, K. L.; Elimelech, M. Fouling and Cleaning of RO Membranes Fouled by Mixtures of Organic Foulants Simulating Wastewater Effluent. *J. Membr. Sci.* **2011**, *376* (1−2), 196−206.

(111) Torres, M. L.; Fernandez, J. M.; Dellatorre, F. G.; Cortizo, A. M.; Oberti, T. G. Purification of Alginate Improves Its Biocompatibility and Eliminates Cytotoxicity in Matrix for Bone Tissue Engineering. *Algal Res.* **2019**, *40*, 101499.

Feed Temperature Effects on Organic Fouling of Reverse Osmosis Membranes: Competition of Interfacial and Transport Properties

Supporting Information

Sara BinAhmed[1], Raymond M. Hozalski[1], Santiago Romero-Vargas Castrillón[1,2,3,*]

Journal: ACS ES&T Engineering

[1] Department of Civil, Environmental, and Geo- Engineering, University of Minnesota,
Minneapolis, MN 55455, USA

[2] Institute for Infrastructure and Environment, School of Engineering,
The University of Edinburgh, William Rankine Building, Thomas Bayes Road,
Edinburgh EH9 3FG United Kingdom

[3] Institute for Materials and Processes, School of Engineering,
The University of Edinburgh, Sanderson Building, Robert Stevenson Road,
Edinburgh EH9 3FB United Kingdom

<u>Contents:</u> 17 pages, including 9 figures and 1 table

*Corresponding author:
Santiago@ed.ac.uk, sromerov@umn.edu. Tel: +44(0)131 651 3567

Supporting Materials and Methods

S.1. Reverse osmosis setup, membrane transport properties and fouling experiments

Reverse osmosis setup. We conducted fouling experiments in a laboratory-scale membrane filtration system comprising a crossflow cell (CF042D, Sterlitech, Kent, WA) with 42-cm^2 active membrane area and a 20-L stainless steel feed tank. The feed temperature was set by a portable chiller (6500 series, Polyscience) equipped with a heat exchange coil immersed in the feed tank. A high-pressure pump (HydraCell M-03S, Wanner Engineering, Minneapolis, MN) circulated the feed solution. The permeate flowrate was recorded with a digital flow meter (SLI-2000, Sensirion, Stäfa, Switzerland) and logged to a computer every 0.2 s. The system was operated in closed-loop mode, recycling the permeate and retentate streams to the feed tank.

Determination of membrane permeance to water. Membranes were compacted with an ultrapure (UP) water (18.2 MΩ cm, Barnstead) feed at 500-580 psi and 25 ˚C until a steady-state permeate flux was observed (typically within ~60 hours). Next, the transmembrane pressure difference was adjusted so that the permeate flux was 20 ± 1 L m^{-2} h^{-1} (LMH), typical of wastewater reclamation by RO,[1,2] at 15.8 cm s^{-1} crossflow velocity. At this stage, the water permeance at 25 °C ($A_{w,25}$) was calculated. Next, the chiller settings were adjusted to maintain the feed at the desired temperature, T = 27, 35, or 40 ˚C, and the pressure difference ($\Delta p_{w,T}$) was reduced to maintain a pure water flux of $J_{w,T} = 20 \pm 1$ LMH at the corresponding temperature T. The system was run overnight to reach steady-state operation at T, after which the water permeance at T ($A_{w,T}$) was calculated using $A_{w,T} = J_{w,T} / \Delta p_{w,T}$.

Fouling experiments. To begin the fouling experiment, the pure water feed was replaced with foulant-free synthetic wastewater (SWW) with the following composition: 0.45 mM KH_2PO_4, 0.935 mM NH_4Cl, 0.5 mM $CaCl_2$, 0.5 mM $NaHCO_3$, 9.20 mM NaCl, and 0.61 mM $MgSO_4$.[3,4] This synthetic wastewater recipe is representative of secondary effluent in certain wastewater treatment plants in California. The system was again allowed to reach steady state at feed temperature T = 27, 35, or 40 ˚C and a baseline permeate flux $J = 20 \pm 1$ LMH. The conductivity of feed and permeate was measured using a conductivity meter with automatic temperature compensation (WD-35604-00, Con 6+ Meter, Oakton) to determine the conductivity rejection coefficient.[4] Finally, the synthetic wastewater feed was supplemented with sodium alginate (SA) foulant solution to initiate the accelerated fouling experiment at an alginate feed concentration of 250 mg L^{-1} while recording the permetate flow for 24 hours. Feed and permeate samples were collected 2 and 24 hours after the addition of alginate to determine conductivity and total organic carbon (TOC) rejection. TOC was measured using a Sievers 900 portable TOC analyzer (GE Analytical Instruments, Boulder, CO) that uses the 5310C National Environmental Methods Index (NEMI) standard method.[5] The feed was diluted 20× before analysis while the permeate was analyzed without dilution.

Fouling of Reverse Osmosis Membranes for Colloidal-Probe AFM. To perform adhesion force measurements over a fouled membrane, an alginate layer was deposited on a pristine membrane using a dead-end filtration cell (Amicon stirred cell 8010, Millipore). To this end, 3 mL of synthetic wastewater (SWW) prepared as described above, supplemented with 50 mg L^{-1} sodium alginate, was filtered through the membrane at 60 psi for 45 minutes.

S.2. Characterization of membrane interfacial properties

Contact angle: The wettability of pristine ESPA2-LD membranes as a function of temperature was evaluated in terms of water contact angle measurements using the sessile drop method. Desiccator-dried membrane coupons were attached to a glass slide using two-sided tape (Scotch®, 3M). A goniometer (DSA30S, Krüss) equipped with a temperature-controlled chamber (TC30) and temperature-controlled liquid dispenser (TC 3212) was used to measure the contact angle of 2-µL water droplets deposited on the membrane substrate. Right-hand-side and left-hand-side angles were determined from digital images using the proprietary ADVANCE software of the instrument for a total of 20 contact angle measurements at each temperature. Measurements were collected at least 15 minutes after both the chamber and UP water reached the set-point temperature ($T = 27$, 35, and 40 ºC). Contact angles were immediately recorded after the 2-µL water drop was deposited.

Roughness: The nanoscale surface roughness of pristine membranes was measured by tapping mode AFM in aqueous solution using an atomic force microscope (MFP-3D-Bio, Asylum Research) equipped with a temperature-controlled fluid cell. AFM scanning was performed in foulant-free synthetic wastewater ($I = 14.7$ mM, see section S.1 or 2.2) at 27, 35, and 40 ºC using SNL-10 probes (cantilever "C", nominal $k = 0.24$ N/m, $f = 56$ kHz, Bruker). The temperature of the fluid cell was increased from ambient to the target temperature $T = 27$, 35, or 40 °C (± 0.2 °C) at a rate of 1 ºC/min. After allowing the AFM to equilibrate at the target temperature for at least an hour, the cantilever resonance frequency was calibrated. Three 5 × 5-µm^2 scans were collected at each temperature at a 0.25 Hz scan rate, after which the root-mean-square (RMS) roughness (R_{RMS}) of 5 random 1 × 1-µm^2 subareas on each image were computed for a total of 15 R_{RMS} values.

Surface charge: An electrokinetic analyzer (SurPASS, Anton Paar) was used to measure the streaming potential of ESPA2 membranes in a 1 mM KCl background electrolyte solution. Two 10 × 20-mm^2 membrane coupons were attached to sample holders of an adjustable gap cell. The electrolyte solution was maintained at a constant temperature (monitored using a thermocouple connected to the electrokinetic analyzer) by placing the solution on a heating stir plate. The zeta potential was calculated from the streaming potential using the Smoluchowski-Helmholtz equation. Prior to the measurements, an instrument validation run was carried out using a cotton cloth (~ 4 × 4 cm^2) following a protocol provided by the manufacturer. Streaming potential data were collected over the pH range 4-10 by addition of aliquots of 0.05 mM NaOH or HCl. Duplicates at each temperature were analyzed. Additional details of zeta potential measurements can be found in our previous work.[6–8]

S.3. Calculation of permeate drag force

The approach loading force (also known as trigger force, Figure S3) exerted on the colloidal probe during AFM force measurements was set to a value representative of the drag force (F_D) exerted on a colloidal particle during membrane filtration. The permeate drag force (F_D) was calculated following the analysis by Goren[9], where the resistance to the approach of a sphere is affected by the permeability of the membrane (considered as a permeable wall).

Goren's analysis[9] leads to the following expression for the permeate drag force,

$$F_\mathrm{D} = -6\pi\mu a_\mathrm{p} J \Phi_\mathrm{H} \qquad \text{(S.1)}$$

where F_D is the permeate drag force (N), and the negative sign indicates that the force is normal to and directed toward the surface of the membrane[10]; μ is the dynamic viscosity of water (kg m^{-1} s^{-1}); a_p is the colloidal probe radius (m); J is the permeate water flux (m s^{-1}); and Φ_H is a hydrodynamic correction factor to Stokes drag force.[9,10]

The hydrodynamic resistance to the particle motion toward the membrane decreases with increasing permeability. When the particle is in contact with the permeable wall, the hydrodynamic correction factor is given by Goren[9] as,

$$\Phi_\mathrm{H} = \left(\frac{2R_\mathrm{m} a_\mathrm{p}}{3}\right)^{\frac{1}{2}} \qquad \text{(S.2)}$$

where $R_\mathrm{m} = \frac{\Delta p}{\mu J}$ is the membrane hydraulic resistance (m^{-1}), and Δp is the transmembrane pressure difference (Pa),

The value of R_m of ESPA2-LD RO membranes was determined experimentally in a laboratory-scale crossflow RO setup operating at a pure water flux $J = 20 \pm 1$ LMH and 25 °C. Three membrane specimens were thus characterized. Flux and corresponding transmembrane pressure values are shown in Table S1. R_m was calculated for each membrane specimen; the resulting values were within the range of typical RO resistance values (5×10^{13} - 1×10^{15} m^{-1}).[11] Using a_p = 2 µm (the radius of the CML particle), Φ_H was calculated using equation S.2 and used to find the drag force from S.1.

Table S1: Experimentally determined pure water flux (J_w), calculated membrane resistance (R_m) and permeate drag force (F_D).

Δp (bar)	**J_w (LMH)**	**R_m (m^{-1})**	**Hydrodynamic Correction Factor Φ_H**	**F_D (nN)**
4.34	20.1	8.73×10^{13}	1.08×10^{4}	2.02
4.83	20.0	9.77×10^{13}	1.14×10^{4}	2.13
4.27	19.6	8.81×10^{13}	1.08×10^{4}	1.98
Average				2.04

S.4. Estimation of the foulant layer thickness and mass of adsorbed alginate

We computed an order-of-magnitude estimate of the mass of alginate adsorbed on the polyamide layer as follows.

The hydraulic resistance due to the foulant (R_f) calculated from our experimental data at 27 °C, under which the most severe fouling is observed, is 0.14 bar L^{-1} m^2 h (140 bar m^{-1} h). This is related to the permeability (P_f) and thickness (l_f) of the alginate film through[12]

$$R_f = \frac{l_f}{P_f} \qquad \text{(R.1)}$$

Olivas et al.[13] reported values of $P_f \sim O(10^{-9})$ g m^{-1} s^{-1} Pa^{-1} = $O(10^{-7})$ m^2 h^{-1} bar^{-1} for the permeability of water vapor in alginate films. Using this value to solve for l_f we obtain,

l_f = (140 bar m^{-1} h)(10^{-7} m^2 h^{-1} bar^{-1}) ~ $O(10^{-5})$ m = 10 μm

This estimate agrees with the thickness of alginate foulant layers ($O(10)$ μm) following RO filtration reported by Xie et al.[14]

Finally, we can estimate the mass of adsorbed alginate (m_f) using the value reported by Kube et al.[15] for the density of alginate ($\rho_f = 0.8755$ g cm^{-3}),

$m_f = \rho_f l_f A_f \approx$ (0.8755 g cm^{-3})(10^{-3} cm)(42 cm^2) = 0.037 g = 37 mg

, where A_f was assumed to be equal to the projected surface area of the membrane (i.e., we assumed complete coverage of the membrane coupon by alginate). Xie et al.[14] reported a *surface* density of alginate foulant layers on RO membranes of ≈ 0.7 mg cm^{-2}; using the same surface area as in our system, this yields an adsorbed mass of alginate of ≈ 30 mg, in good agreement with our estimate based on l_f and ρ_f.

These calculations show that the mass of adsorbed alginate is ca. 3% of the mass of alginate available in the bulk solution (i.e., 0.25 g L^{-1} × 4 L = 1 g). We therefore conclude that the slow-down of the rate of fouling is not due to a lower concentration of foulant in the feed. Rather, the decreasing rate of flux loss results from weakly adhesive or repulsive foulant-foulant interactions (Figure 3).

Supporting Results

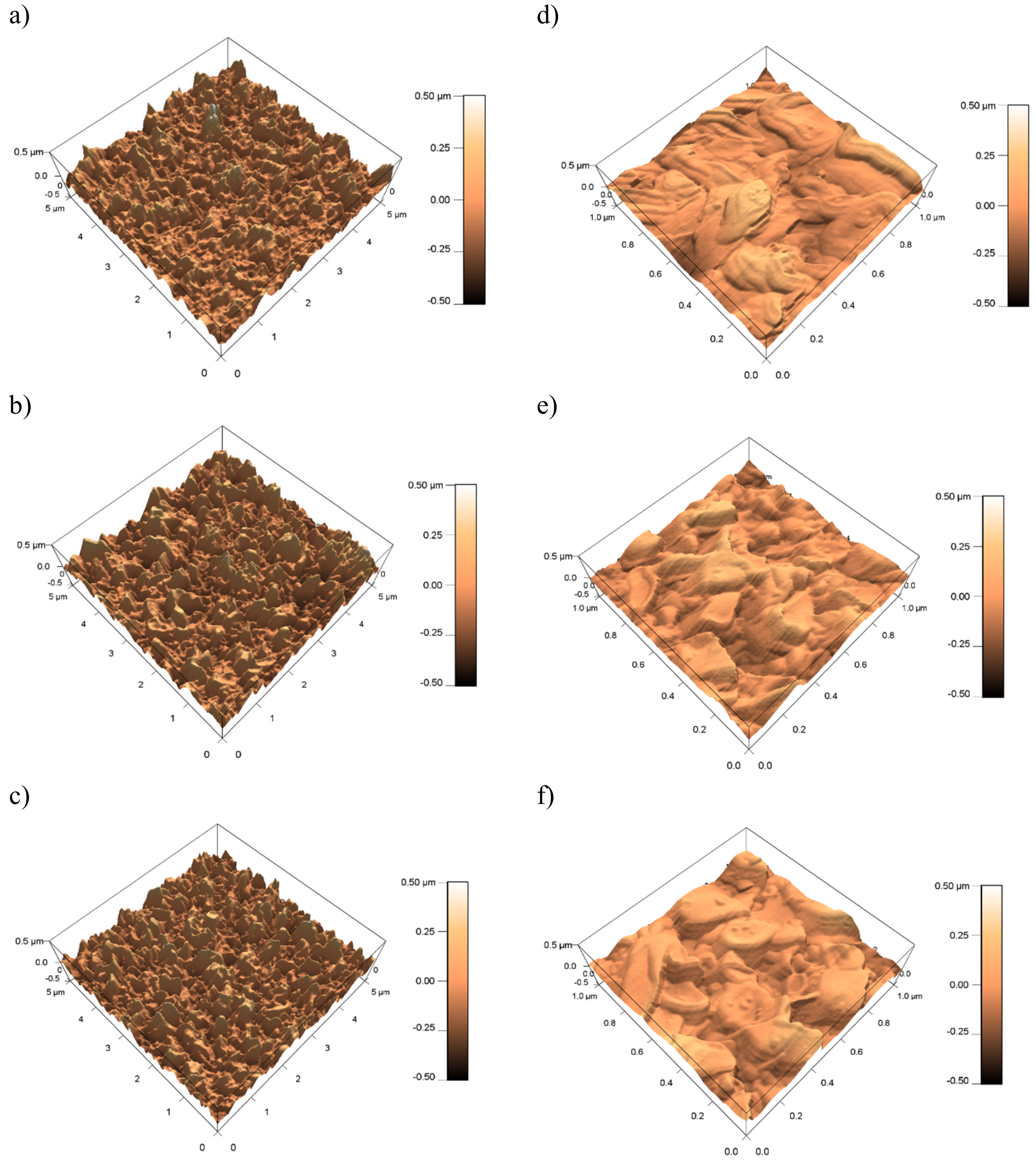

Figure S1: Tapping mode AFM images of pristine ESPA2-LD membranes scanned in foulant-free synthetic wastewater (pH 7.4; *I* = 14.7 mM) at 27 °C (a, d), 35 °C (b, e), and 40 °C (c, f). Left column: 5 × 5 µm^2 scan area. Right column: 1 × 1 µm^2 scan area.

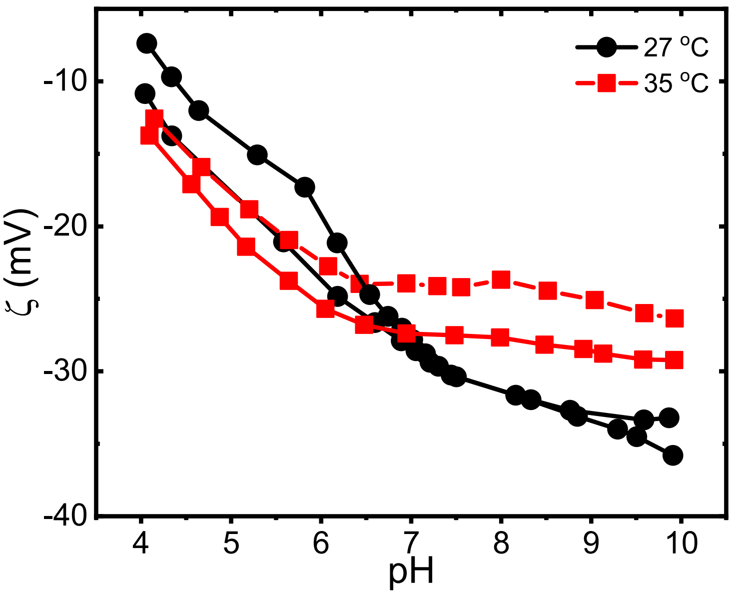

Figure S2: Zeta potential (ζ) of pristine ESPA2-LD membranes at 27 °C and 35 °C determined in 1 mM KCl solution. Duplicates are shown at each temperature.

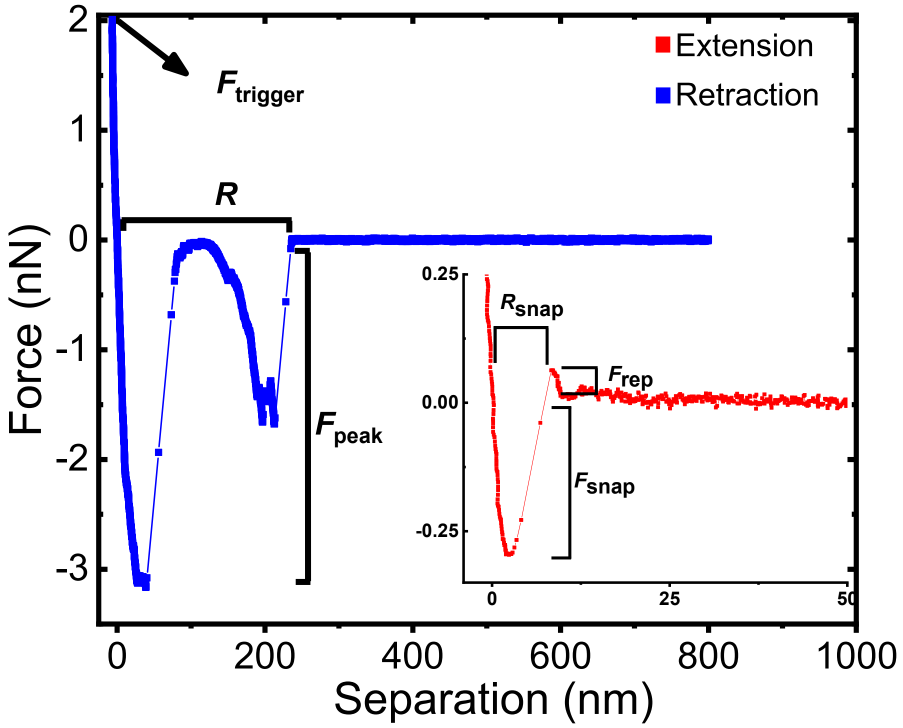

Figure S3: Representative retraction force curve and approach force curve (shown in the inset) of a CML colloidal probe on a pristine ESPA2-LD membrane at 27 °C. Data were collected in synthetic wastewater supplemented with 20 mg L^{-1} sodium alginate ($t_{contact}$ = 5 s; $F_{trigger}$ = 2 nN; pH 7.4; I = 14.7 mM). The curve shows the definition of the peak adhesion force (F_{peak}), snap-in force (F_{snap}), trigger force ($F_{trigger}$), rupture separation (R), snap-in separation (R_{snap}), and repulsive force (F_{rep}). The units of the x- and y-axes in the inset are nm and nN, respectively.

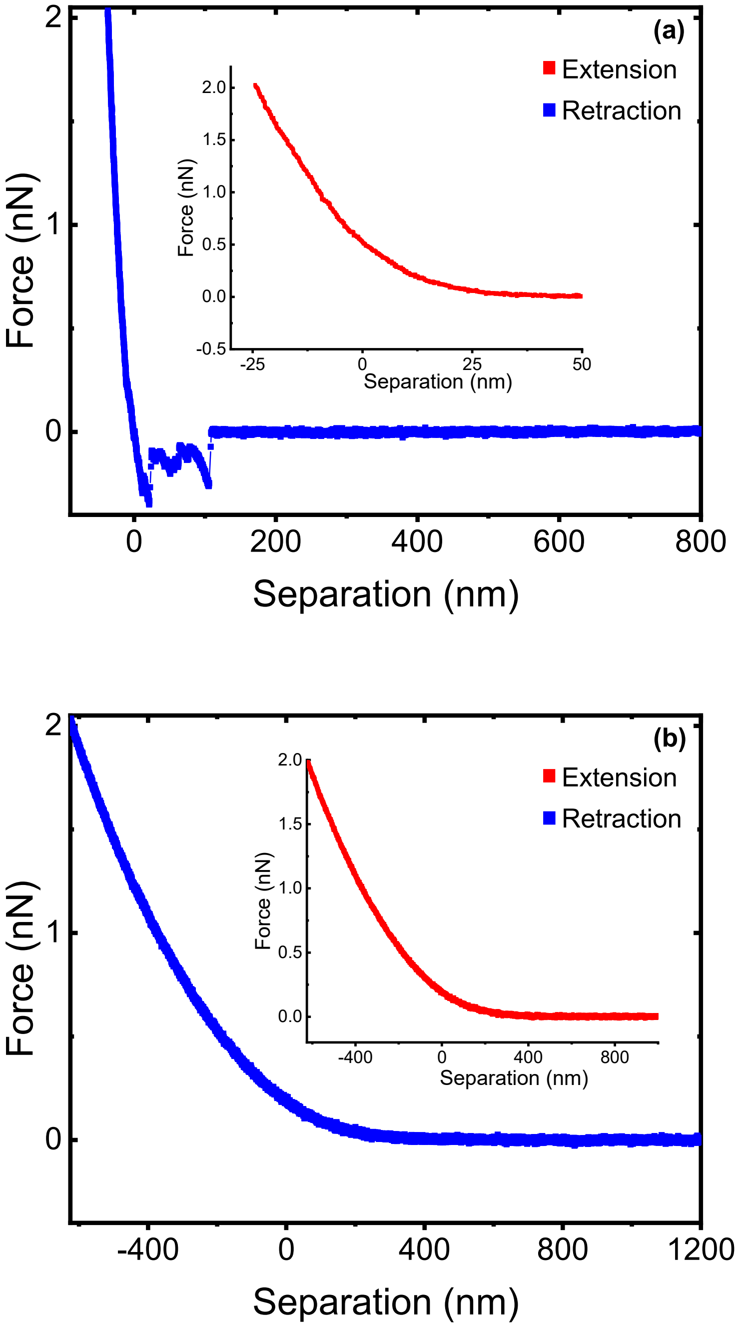

Figure S4: Representative retraction and approach force curves (the latter shown in the inset) of a CML colloidal probe on an alginate-fouled ESPA2-LD membrane at 27 °C. Panel (a) shows a typical force curve exhibiting repulsive interactions during extension, and weak adhesion during retraction. Panel (b) shows the case of repulsive interactions during extension and retraction. Data were collected in synthetic wastewater supplemented with 20 mg L^{-1} sodium alginate ($t_{\mathrm{contact}} = 5$ s; $F_{\mathrm{trigger}} = 2$ nN; pH 7.4; $I = 14.7$ mM).

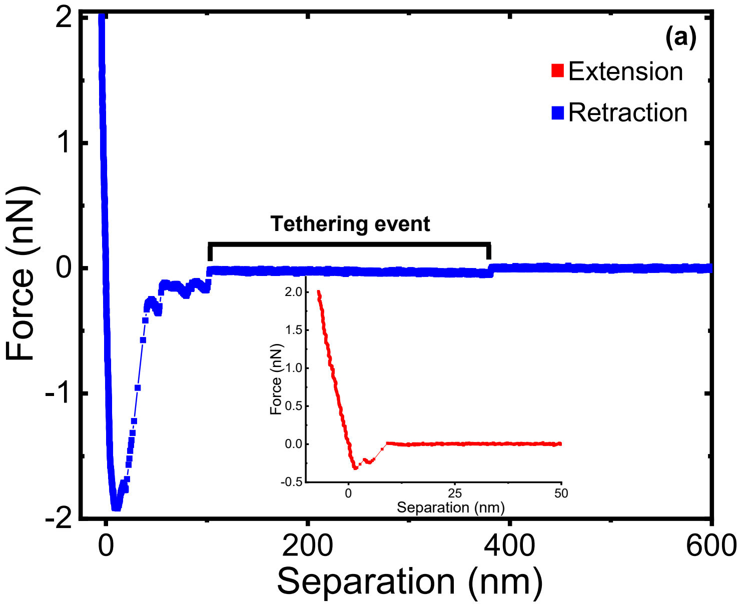

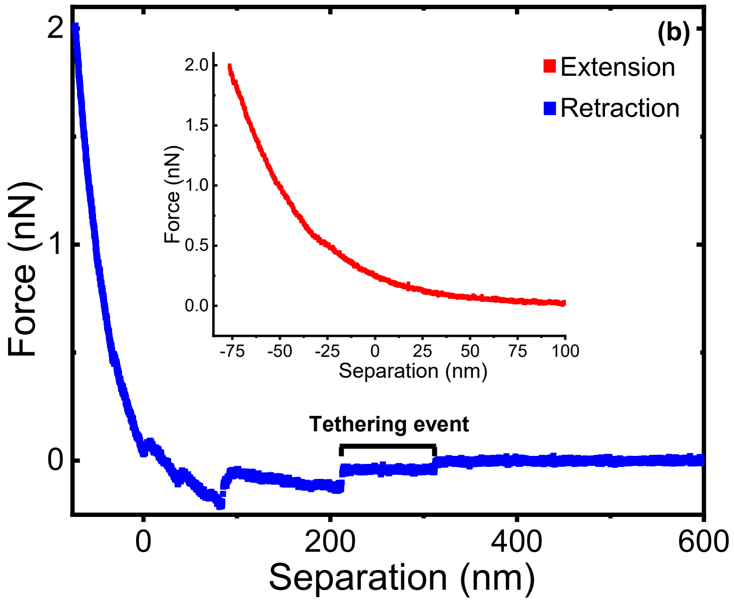

Figure S5: Representative retraction force curve exhibiting a tethering event during adhesion of a CML colloidal probe at 27 °C on an ESPA2-LD (a) pristine and (b) alginate-fouled membrane (approach force curves shown in the inset). Data were collected in synthetic wastewater supplemented with 20 mg L^{-1} sodium alginate ($t_{\text{contact}} = 5$ s; $F_{\text{trigger}} = 2$ nN; pH 7.4; $I = 14.7$ mM).

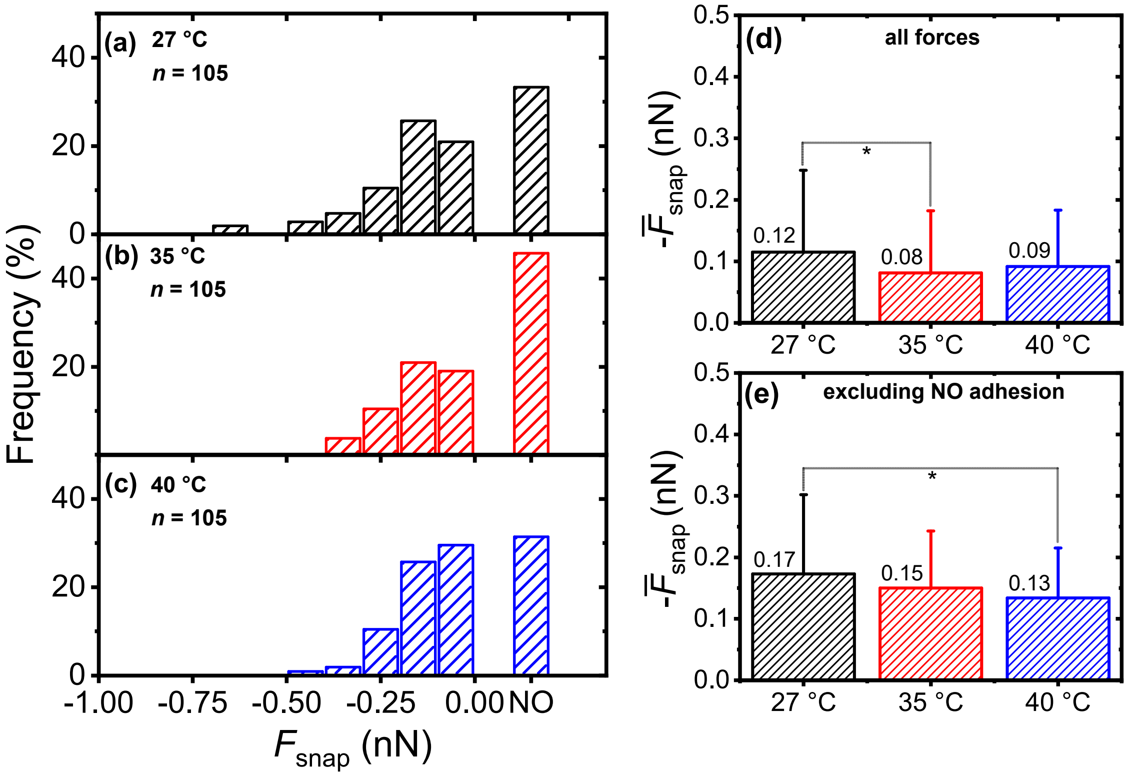

Figure S6: (a-c) Distribution of snap-in forces during adhesion of a CML colloidal probe to pristine ESPA2-LD membranes for each indicated temperature (given in the inset along with the number of force measurements, *n*). Force curves in which snap-in events were not detected are tallied as the "NO" column. (d) Average snap-in force ($\bar{F}_{\text{snap}}$) at each temperature calculated from (a-c) including the non-adhesive (i.e., purely repulsive approach) events as $\bar{F}_{\text{snap}} = 0$ (* denotes statistical significance with $p < 0.05$). (e) Average snap-in force ($\bar{F}_{\text{snap}}$) at each temperature calculated from (a-c) excluding the non-adhesive events (* denotes statistical significance with $p < 0.05$). Error bars denote one standard deviation. Data were collected in synthetic wastewater supplemented with 20 mg L^{-1} sodium alginate ($t_{\text{contact}} = 5$ s; $F_{\text{trigger}} = 2$ nN; pH 7.4; $I = 14.7$ mM).

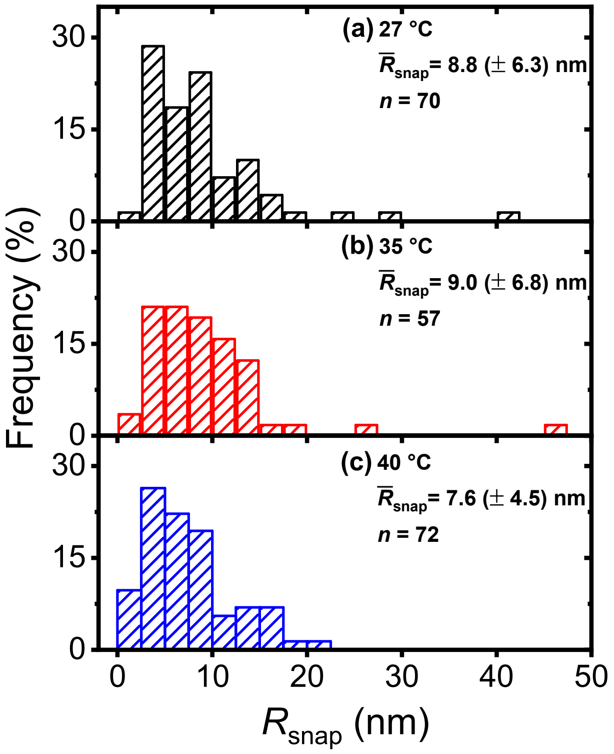

Figure S7: Distribution of snap-in distances (R_{snap}) during adhesion of a CML colloidal probe to pristine ESPA2-LD membranes. Data were collected in synthetic wastewater supplemented with 20 mg L^{-1} sodium alginate at each indicated temperature (given in the inset along with the number of measurements (n) and average snap-in distance $\bar{R}_{snap}$ (± standard deviation)). Other experimental details: $t_{contact}$ = 5 s; $F_{trigger}$ = 2 nN; pH 7.4; I =14.7 mM. Average snap-in distances are similar at all temperatures ($p > 0.05$ for all pairwise comparisons).

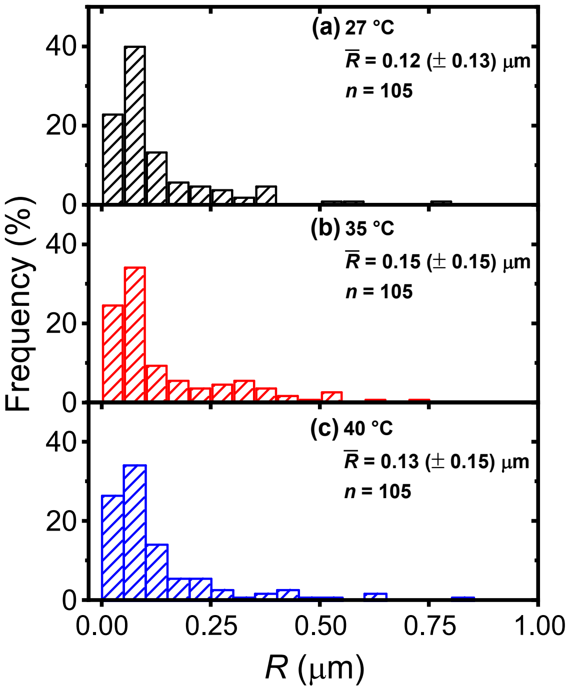

Figure S8: Distribution of rupture separations (*R*) during adhesion of a CML colloidal probe to pristine ESPA2-LD membranes. Data were collected in synthetic wastewater supplemented with 20 mg L^{-1} sodium alginate at each indicated temperature (given in the inset along with the number of measurements (*n*) and average rupture separation $\bar{R}$ (± standard deviation)). Other experimental details: $t_{\text{contact}} = 5$ s; $F_{\text{trigger}} = 2$ nN; pH 7.4; I =14.7 mM. Average rupture separations are similar at all temperatures ($p > 0.05$ for all pairwise comparisons).

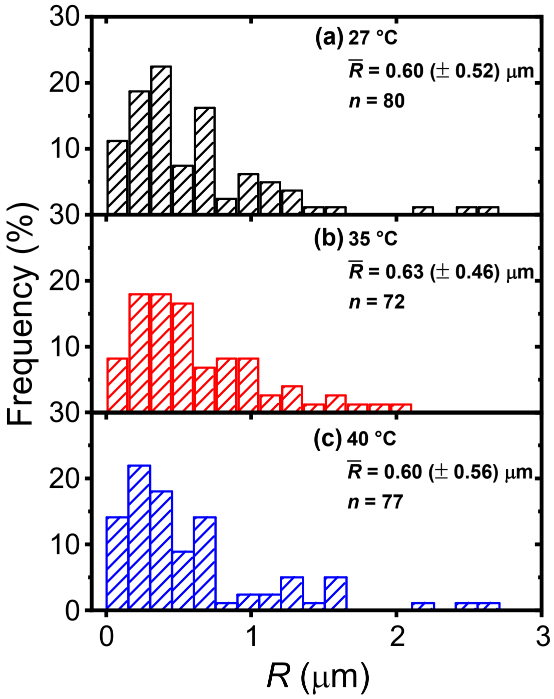

Figure S9: Distribution of rupture separations (R) during adhesion of a CML colloidal probe to alginate-fouled ESPA2-LD membranes. Data were collected in synthetic wastewater supplemented with 20 mg L^{-1} sodium alginate at each indicated temperature (given in the inset along with the number of measurements (n) and average rupture separation $\bar{R}$ (± standard deviation)). Other experimental details: $t_{\text{contact}} = 5$ s; $F_{\text{trigger}} = 2$ nN; pH 7.4; I =14.7 mM. Average rupture separations are similar at all temperatures ($p > 0.05$ for all pairwise comparisons).

References

(1) Fujioka, T.; Khan, S. J.; McDonald, J. A.; Henderson, R. K.; Poussade, Y.; Drewes, J. E.; Nghiem, L. D. Effects of Membrane Fouling on N-Nitrosamine Rejection by Nanofiltration and Reverse Osmosis Membranes. *J. Memb. Sci.* **2013**, *427*, 311–319. https://doi.org/10.1016/j.memsci.2012.09.055.

(2) Fujioka, T.; Khan, S. J.; McDonald, J. A.; Roux, A.; Poussade, Y.; Drewes, J. E.; Nghiem, L. D. N-Nitrosamine Rejection by Reverse Osmosis: Effects of Membrane Exposure to Chemical Cleaning Reagents. *Desalination* **2014**, *343*, 60–66. https://doi.org/10.1016/j.desal.2013.10.032.

(3) Tiraferri, A.; Kang, Y.; Giannelis, E. P.; Elimelech, M. Superhydrophilic Thin-Film Composite Forward Osmosis Membranes for Organic Fouling Control: Fouling Behavior and Antifouling Mechanisms. *Environ. Sci. Technol.* **2012**, *46* (20), 11135–11144. https://doi.org/10.1021/es3028617.

(4) Herzberg, M.; Elimelech, M. Biofouling of Reverse Osmosis Membranes: Role of Biofilm-Enhanced Osmotic Pressure. *J. Memb. Sci.* **2007**, *295* (1–2), 11–20. https://doi.org/10.1016/j.memsci.2007.02.024.

(5) *Standard Methods for the Examination of Water and Wastewater*, 22nd ed.; Rice, E. W., Baird, R. B., Eaton, A. D., Clesceri, L. S., Eds.; American Public Health Association, American Water Works Association, Water Environment Federation, 2012.

(6) Xue, J.; BinAhmed, S.; Wang, Z.; Karp, N. G.; Stottrup, B. L.; Romero-Vargas Castrillón, S. Bacterial Adhesion to Graphene Oxide (GO)-Functionalized Interfaces Is Determined by Hydrophobicity and GO Sheet Spatial Orientation. *Environ. Sci. Technol. Lett.* **2018**, *5* (1), 14–19. https://doi.org/10.1021/acs.estlett.7b00509.

(7) Binahmed, S.; Hasane, A.; Wang, Z.; Mansurov, A.; Romero-Vargas Castrillón, S. Bacterial Adhesion to Ultrafiltration Membranes: Role of Hydrophilicity, Natural Organic Matter, and Cell-Surface Macromolecules. *Environ. Sci. Technol.* **2018**, *52* (1), 162–172. https://doi.org/10.1021/acs.est.7b03682.

(8) Wuolo-Journey, K.; Binahmed, S.; Linna, E.; Romero-Vargas Castrillón, S. Do Graphene Oxide Nanostructured Coatings Mitigate Bacterial Adhesion? *Environ. Sci. Nano* **2019**, *6* (9), 2863–2875. https://doi.org/10.1039/c9en00499h.

(9) Goren, S. L. The Hydrodynamic Force Resisting the Approach of a Sphere to a Plane Permeable Wall. *Colloid Interface Sci.* **1979**, *69* (1), 78–85.

(10) Kang, S.; Subramani, A.; Hoek, E.; Deshusses, M.; Matsumoto, M. Direct Observation of Biofouling in Cross-Flow Microfiltration: Mechanisms of Deposition and Release. *J. Memb. Sci.* **2004**, *244* (1–2), 151–165. https://doi.org/10.1016/j.memsci.2004.07.011.

(11) Benjamin, M. M.; Lawler, D. F. Membrane Processes. In *Water Quality Engineering Physical/Chemical Treatment Processes*; John Wiley & Sons, Inc.: Hoboken, NJ, 2013; pp 731–845.

(12) Sagle, A. C.; Van Wagner, E. M.; Ju, H.; McCloskey, B. D.; Freeman, B. D.; Sharma, M. M. PEG-Coated Reverse Osmosis Membranes: Desalination Properties and Fouling Resistance. *J. Memb. Sci.* **2009**. https://doi.org/10.1016/j.memsci.2009.05.013.

(13) Olivas, G. I.; Barbosa-Cánovas, G. V. Alginate-Calcium Films: Water Vapor Permeability and Mechanical Properties as Affected by Plasticizer and Relative Humidity. *LWT - Food Sci. Technol.* **2008**, *41* (2), 359–366. https://doi.org/10.1016/j.lwt.2007.02.015.

(14) Xie, M.; Lee, J.; Nghiem, L. D.; Elimelech, M. Role of Pressure in Organic Fouling in Forward Osmosis and Reverse Osmosis. *J. Memb. Sci.* **2015**, *493*, 748–754.

https://doi.org/10.1016/j.memsci.2015.07.033.

(15) Kube, M.; Mohseni, A.; Fan, L.; Roddick, F. Impact of Alginate Selection for Wastewater Treatment by Immobilised Chlorella Vulgaris. *Chem. Eng. J.* **2019**, *358*, 1601–1609. https://doi.org/10.1016/j.cej.2018.10.065.